



The Abdus Salam
International Centre for Theoretical Physics



SMR/1758-8

**"Workshop on Ion Beam Studies of Nanomaterials:
Synthesis, Modification and Characterization"**

26 June - 1 July 2006

Controlled ion beam synthesis of nanoclusters in glasses

*H. Bernas
Institut de Physique Nucleaire (I.P.N.)
& Laboratoire de Physique des Solides
Orsay, France*



How chemistry affects the ion beam synthesis of PbS nanocrystals

R. Espiau de Lamaestre^{a,b,*}, H. Bernas^a, Ch. Ricolleau^c, J. Majimel^d

^a CSNSM/CNRS, Université Paris Sud, 91405 Orsay Campus, France

^b Fontainebleau Research Center, Corning SA, 77210 Avon, France

^c LPS/CNRS, 75231 Paris Cedex 5, France

^d CECM/CNRS, 94407 Vitry-sur-Seine, France

Available online 21 October 2005

Abstract

Solid state chemical reactions involving the multiple oxidation states of sulfur are shown to dominate the synthesis of PbS nanocrystals in pure silica via co-implantation and annealing. The formation of PbSO₄ as well as PbS nanocrystals and small amorphous clusters is evidenced, and related to atomic transport occurring during annealing. A mechanism is proposed.

© 2005 Elsevier B.V. All rights reserved.

PACS: 85.40.Ry; 78.67.-n; 61.46.+w; 61.14.-x

Keywords: Implantation; TEM; SIMS; PbS nanocrystal; Oxidation state

1. Introduction

The optical properties of narrow-gap semiconducting nanocrystals such as PbS in glass or silica are of considerable current interest, as regards both basic physics [1] and applications [2]. PbS nanocrystals have been synthesized in glasses by introducing the components of the nanocrystals directly into the melt, cooling and subsequently heating to promote some control over nanocrystal growth [3]. Nanocrystalline PbS was also synthesized by high fluence ($2.5\text{--}7.5 \times 10^{16}$ at. cm⁻², Pb at about 300 keV and S at about 80 keV) co-implantation of Pb and S into pure silica and annealing at 1000 °C [4–7], but the size distribution was large and bimodal. The present work offers an explanation of the latter results. We show that the nucleation and growth of PbS nanocrystals are largely determined by Pb and S redox properties in silica. In crystalline PbS, the formal oxidation state of Pb is usually (+II), that of S (–II).

On the other hand, Pb in glasses is commonly in the (+II) oxidation state, whereas S oxidation states range from (–II) to (+VI). A whole range of chemical reactions can therefore combine sulfur with Pb (and/or preexisting PbS clusters) to form PbS nanocrystals, threatening growth control. We show that ion implantation cannot circumvent the chemical interaction between the implanted elements and the host, and that this interaction is crucial in the early stages of growth.

2. Experimental

Pure silica was co-implanted with S (100 keV, 2×10^{15} at. cm⁻²) and Pb (480 keV, 2×10^{15} at. cm⁻²), with the IRMA facility [8]. Diffusion and solubility properties were monitored by SIMS profiling after systematic sample anneals ranging from 800 to 900 °C in a quartz tube furnace under dry N₂. Both medium and high resolution transmission electron microscopy (TEM) was performed on the samples, as well as photoluminescence (PL) experiments with a 488 nm/365 mW argon laser chopped at 53 Hz and PL signal detection by a cooled PbS detector using a lock-in amplifier.

* Corresponding author. Address: CSNSM/CNRS, Université Paris Sud, 91405 Orsay Campus, France. Tel.: +33 16915 5262; fax: +33 16915 5268.

E-mail address: espiau@csnsm.in2p3.fr (R. Espiau de Lamaestre).

3. Results and discussion

After co-implantation and annealing at 850 °C for 1 h, TEM (Fig. 1(a)) revealed the growth of large contrasted precipitates surrounded by numerous small ones (size < 2 nm). Annealed samples exhibited a strong PL in the wavelength range 1.2–2.2 μm (Fig. 2), shifting to higher wavelengths at longer anneals, hence presumably related to exciton recombination in the nanocrystals.

Two different precipitate structures were found by HRTEM: the expected cubic $Fm\bar{3}m$ ($a = b = c = 5.94 \text{ \AA}$) structure (Fig. 1(b)) and a structure with spacing close to $d = 2.75 \text{ \AA}$, observed in 1/5 of the precipitates. An axis zone showed this lattice spacing together with two directions of order two and an extinction in one of them (Fig. 1(c)). We ascribe it to the orthorhombic $PbSO_4$ phase (space group $Pbnm$, $a = 6.959 \text{ \AA}$, $b = 8.482 \text{ \AA}$, $c = 5.398 \text{ \AA}$) [9]. In $PbSO_4$, sulfur is in the (+VI) formal oxidation state, whereas in PbS it is in the (–II) state. About 40% of observed precipitates are polycrystalline and mostly $PbSO_4$. The latter composition is favored by the simultaneous existence of different sulfur oxidation states (+VI/–II) during nanocrystal formation, polycrystallinity being due to fast quenching from melted nanocrystals after anneal.

Numerous small clusters of size < 2 nm are found: they exhibit no lattice fringes under HRTEM, indicating that they are amorphous; their chemical nature is unknown. They are separated from the $PbS/PbSO_4$ nanocrystals by a depleted layer (not shown), suggesting that small clusters dissolve progressively, contributing to the growth of surrounding larger $PbS/PbSO_4$ nanocrystals. No PL is detected at wavelengths below 1 μm (Fig. 2), confirming the absence of small PbS nanocrystals.

We have shown elsewhere [10] that PbS ($PbSO_4$) precipitation is controlled by the less-concentrated element (either Pb or S, O being ubiquitous in silica), and that the diffusion behavior of sulfur depends strongly on its redox state. Most implanted sulfur atoms are in the immobile (–II) state, a small proportion being in the very mobile (+VI) state. The latter is responsible for growth outside of the implanted profile, i.e. partial loss of growth depth control. This difference in mobility, originating from chemical interactions of sulfur with the silica host, leads to multiple chemical routes for the synthesis of PbS as exemplified by the formation of $PbSO_4$ nanocrystals. Reduced (–II) sulfur has the same oxidation state as in PbS , but is not very mobile since it is usually in polysulfide form in oxide glasses [11]: hence, it is not obvious that it participates directly in PbS growth reactions.

We propose the following scenario for initial growth. The numerous small, amorphous clusters observed prior to nanocrystal growth could be chemical combinations of Pb and polysulfides. The latter's low mobility inhibits nanocrystal growth. When SO_3 diffusion sets in (higher annealing temperatures/longer annealing times), growth of PbS and/or $PbSO_4$ occurs by the reactions: $PbO + SO_3 \rightarrow PbSO_4 \leftrightarrow PbS + 2O_2$ or $PbO + SO_3 \rightarrow PbS + 2O_2$.

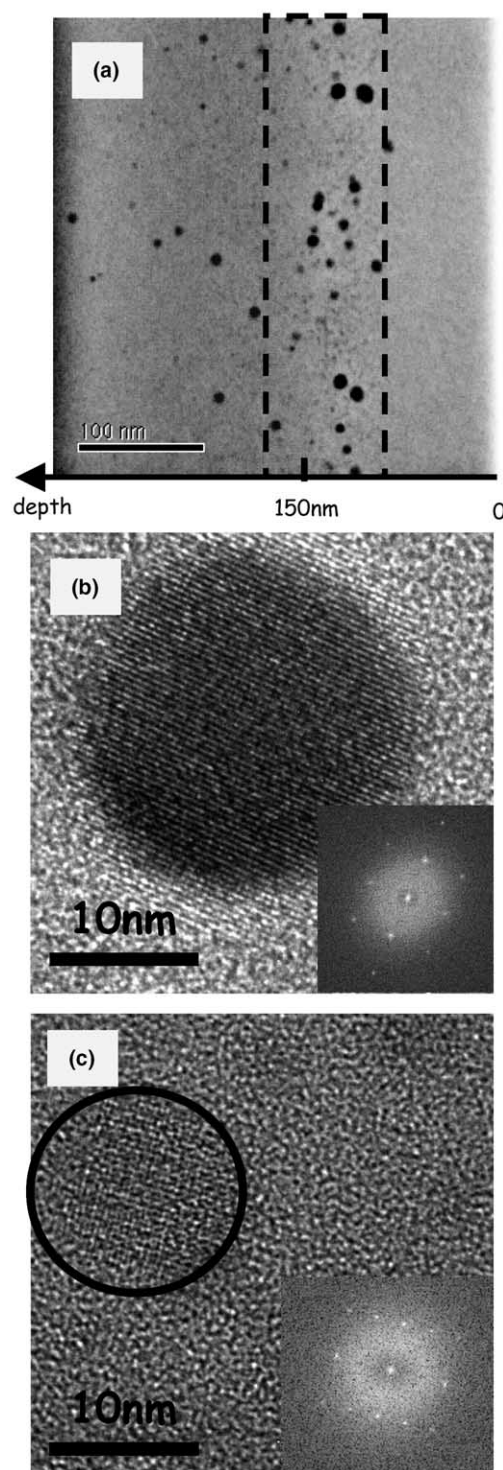


Fig. 1. (a) TEM image of Pb + S co-implanted silica, after annealing at 850 °C for 1 h. Hatched lines show the implanted depth range. Precipitates outside of this zone are due to sulfur diffusion (see text and [9]). (b, c): HRTEM images from Pb and S co-implanted sample annealed at 850 °C for 1 h; (b) [1 0 0] axis zone image of a cubic PbS nanocrystal. Inset is the image FFT; (c) [1 2 0] axis zone image of orthorhombic $PbSO_4$ nanocrystal. Inset is the image FFT.

The freed oxygen help to dissolve polysulfides into mobile SO_3 groups (e.g. $S^{2-} + 2O_2 \rightarrow SO_3 + O_{glass}^{2-}$), which may

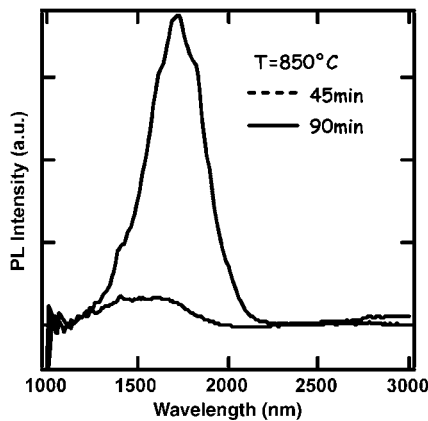


Fig. 2. PL spectra of Pb + S co-implanted silica annealed at 850 °C for different times.

then participate in growth. This is consistent with progressive dissolution of small amorphous precipitates into surrounding nanocrystals. Nucleation of PbS/PbSO₄ would then be controlled by the dissolution kinetics of the amorphous clusters, and this may account both for the observed nanocrystal size distribution broadening and for the difference between initial implant profiles and final nanocrystal depth distribution.

4. Conclusions

We have shown that controlling compound semiconductor nanocrystal formation by implantation is not straightforward, and cannot rely simply on initial implantation profiles and nonequilibrium states. One has to consider: (i) the diffusion properties of the individual components – for example in our case, the fact that sulfur has at least two different oxidation states with very different mobilities; (ii) the diffusion interactions (through their chemical affinity) between the two components of the nanocrystals; (iii)

chemical reactions between the nanocrystal and host components (notably oxygen). The second effect may be emphasized at higher implantation fluences, due to steeper concentration gradients. Similar redox and diffusion effects are likely also important in other chalcogenide nanocrystals' syntheses by ion implantation.

Acknowledgment

We are grateful to O. Kaitasov and S. Collin for assistance with ion implantation and TEM sample preparation.

References

- [1] S.V. Gaponenko, *Optical Properties of Semiconductor Nanocrystals*, Cambridge University Press, 1999.
- [2] For example, G. Tamulaitis, V. Gulbinas, G. Kodis, A. Dementjev, L. Valkunas, I. Motchalov, H. Raaben, *J. Appl. Phys.* 88 (1) (2000) 178.
- [3] N.F. Borelli, D.W. Smith, *J. Non-Cryst. Solids* 180 (1994) 25.
- [4] A. Meldrum, S.P. Withrow, R.A. Zuhr, C.W. White, L.A. Boatner, J.D. Budai, I.M. Anderson, D.O. Henderson, M. Wu, A. Ueda, R. Mu, *Microcrystall. Nanocrystall. Semicond.* 1998 (1999) 317.
- [5] A. Meldrum, E. Sonder, R.A. Zuhr, I.M. Anderson, J.D. Budai, C.W. White, L.A. Boatner, D.O. Henderson, *J. Mater. Res.* 14 (12) (1999) 4489.
- [6] C.W. White, J.D. Budai, A.L. Meldrum, S.P. Withrow, R.A. Zuhr, E. Sonder, A. Puzeky, D.B. Geohegan, J.G. Zhu, D.O. Henderson, *Atomistic Mechanisms in Beam Synthesis and Irradiation of Materials*, Mater. Res. Soc, Warrendale, PA, USA, 1999, p. 399.
- [7] A. Meldrum, C.W. White, L.A. Boatner, I.M. Anderson, R.A. Zuhr, E. Sonder, J.D. Budai, D.O. Henderson, *Nucl. Instr. and Meth. B* 148 (1999) 957.
- [8] J. Chaumont, F. Lalu, M. Salomé, *Nucl. Instr. and Meth.* 189 (1981) 193.
- [9] M. Miyake, I. Minato, H. Morikawa, S.I. Iwai, *Am. Mineral.* 63 (1978) 506.
- [10] R. Espiau de Lamaestre, H. Bernas, F. Jomard, *Nucl. Instr. and Meth. B* 216 (2004) 402.
- [11] M.B. Volf, *Chemical Approach to Glass*, Elsevier Science, New York, 1984, p. 524.

Synthesis of Lead Chalcogenide Nanocrystals by Sequential Ion Implantation in Silica

R. Espiau de Lamaestre,^{†,‡} J. Majimel,[§] F. Jomard,^{||} and H. Bernas^{*,†}

CSNSM/CNRS, Université Paris Sud, 91405 Orsay Campus, France, Fontainebleau Research Center, Corning SAS, 77210 Avon, France, CECM/CNRS, 94407 Vitry-sur-Seine, France, and LPSC/CNRS, 92195 Meudon Cedex, France

Received: May 23, 2005; In Final Form: July 18, 2005

Lead chalcogenide (PbS, PbSe, and PbTe) nanocrystals were synthesized by sequential implantation of Pb and one of the chalcogen species into pure silica. The implantation energy and fluence were chosen so that the implantation profiles practically overlap at a depth ≈ 150 nm with a maximum concentration of about 0.3 atom %. Annealing for 1–8 h at 850–900 °C triggers nanocrystal growth, which is monitored by high-resolution (HRTEM) and conventional transmission electron microscopy (TEM), secondary-ion mass spectrometry (SIMS), and Rutherford backscattering spectrometry (RBS). Striking differences are found in the depth distributions and microstructures of the resulting nanocrystals. We show that the differing chemical interactions of Pb and chalcogens (between each other and with silica) play a crucial role in chalcogenide nucleation and growth. Using available information on chalcogen redox states in silicate glass, we propose a nonclassical nucleation and growth mechanism consistent with our experimental results. The complex chemistry involved at the microscopic level is shown to impair control over the nanocrystal size distribution. Finally, PbS nanocrystal-doped silica is shown to emit intense photoluminescence (PL) in the 1.5–2 μm wavelength range, an effect that we relate to the above nucleation and growth scheme.

1. Introduction

Lead chalcogenide nanocrystals have been synthesized in glasses by various routes. The earliest one consists of introducing the components directly into the glass melt. After pouring and cooling of the glass, subsequent heating promotes a more or less controlled growth of nanocrystals. The method has been successfully applied to chalcogenide nanocrystal synthesis in various types of glasses: PbS (silicate glass),¹ PbSe (phosphate glass),^{2,3} and PbTe (borosilicate⁴ and silicate⁵ glasses). Synthesis control can usually only be achieved in rather limited composition and temperature ranges.

An apparently efficient way to overcome compositional limitations is to use the ion implantation technique to force solubility in any desired matrix. The use of ion beams with controlled energy and fluence obviously provides control over the initial dopants' depth distribution and concentration. Does it also lead to control over nanocrystal sizes and spatial distributions after the required postimplant annealing? Only PbS nanocrystal synthesis had been reported so far, via sequential implantation of Pb and S at high fluences ($2.5\text{--}7.5 \times 10^{16}$ $\text{at}\cdot\text{cm}^{-2}$) into pure silica, followed by annealing at 1000 °C.^{6–9} However, the size distribution was often found to be bimodal and uncontrolled. It is improved when going to low doses,⁷ but size distributions remain rather broad and close to a log-normal shape. We have shown¹⁰ that such lack of control must be related to the chemical interaction of sulfur with pure silica, which strongly influences S diffusion properties¹¹ as well as the

composition and structure of growing nanocrystals.¹² Here, we extend our previous studies of PbS formation to other ion implantation and annealing conditions and study PbSe and PbTe nanocrystal formation conditions as well. We show that the growth characteristics (crystalline structure, precipitation depth) of lead chalcogenide nanocrystals grown by annealing of sequentially implanted pure silica may be interpreted in terms of differences in the chalcogen chemical properties. We offer answers to the following questions: What is the chemical nature of the chalcogenide nanocrystals formed in this way? What is their nucleation mechanism? What is the influence of the chalcogen chemical state(s) on growth, and especially on size and depth control?

2. Chemistry of Chalcogens and Chalcogenides in Glasses

The chalcogen formal redox states generally range from –II to +VI, depending on the concentration and redox interaction with their host.¹³ Such effects dominate in implanted glasses despite the latter's initially nonequilibrium character, simply because nanocrystal formation requires annealing at sufficiently high temperatures. Although they are in the same column of the periodic table, chemical properties vary when switching from S to Se, and even more so from Se to Te. Under given redox conditions (glass composition, temperature, and composition of the annealing atmosphere), they will be present in differing states. In silicate glasses, S may be found in –II to +VI redox states, whereas Se and Te are in –II, 0, and +IV states. Oxidized forms are usually very mobile and volatile (e.g., the glass transition temperatures of SeO_2 and TeO_2 are, respectively, 317 °C and 450 °C). Reduced –II forms are usually encountered as polychalcogenides, thus hindering their potential diffusion, and Te very often occurs as metallic precipitates. Among the three chalcogens, S is the one that has been most studied¹⁴ for technological reasons.

* Corresponding author. E-mail: bernas@csnsm.in2p3.fr. Telephone: +33 16915 5222. Fax: +33 16915 5268.

[†] CSNSM/CNRS, Université Paris Sud.

[‡] Fontainebleau Research Center, Corning SAS.

[§] CECM/CNRS.

^{||} LPSC/CNRS.

TABLE 1: E Is the Implantation Energy, R_p the Projected Range, and $fwhm$ the Full Width at Half-Maximum of the Implantation Profile, According to SRIM Simulations.^a

	S	Pb	Se	Te	Pb
E (keV)	100	480	210	300	480
fluence (10^{15} at \cdot cm $^{-2}$)	2.2	1.4	1.5	1.35	1
R_p (nm)	136	144	141	140	144
$fwhm$ (nm)	108	67	101	87	67
max concentration (atom %)	0.30	0.30	0.21	0.23	0.22
annealing time (h)	1				
annealing temperature ($^{\circ}$ C)	800–950				

^a Also listed are the maximum concentrations at depth R_p , assuming an atomic density 6.5×10^{22} at \cdot cm $^{-3}$ (i.e., 2.17 g \cdot cm $^{-3}$) for SiO $_2$.

The influence of these chemical properties on the chalcogen diffusion properties is quite drastic.¹¹ The behavior of implanted Se is somewhat similar to that of implanted S, with the overwhelming fraction being in the immobile reduced form, while a small oxidized fraction (concentration below 100 apm) is very mobile. However, the oxidized form of Se may actually be in the +IV redox state (SeO $_2$), whereas that of S is more likely in the +VI state (SO $_3$),¹³ and their diffusion coefficients differ by one to 2 orders of magnitude, that of oxidized selenium being lower than that of oxidized sulfur.¹¹ Implanted Te is mainly in the atomic state and precipitates as Te metal upon annealing.¹¹ Because of their chemical interaction, chalcogen motion in turn has a major effect on Pb motion. As first shown in ref 12 and 15, the chemical state of sulfur not only determines the chemical nature of the precipitated phase but also the depth distribution of the nanocrystals via the Pb–chalcogen correlated diffusion properties. This is detailed below. We consequently expect, and find, significant differences in nucleation and growth behavior depending on the chalcogens that combine with Pb.

3. Experimental Section

It was previously shown^{6–9} that PbS cluster nucleation and early growth occur during implantation above concentrations around 10^{21} at cm $^{-3}$. We thus restrict our studies to lower concentrations so as to observe precipitation from the earliest stage and also to enhance experimental accuracy in depth and radius distribution determination.

Pure Corning silica was sequentially implanted with Pb and one of the chalcogens at concentrations well below the aforementioned threshold (Table 1). Implantations were performed with the IRMA facility¹⁶ at CSNSM. Using the standard SRIM code,¹⁷ energies (and fluences) were chosen so that the projected range (and concentration at maximum) of both lead and the chalcogen would coincide. Rutherford backscattering (RBS) experiments were performed in a number of cases, using the ARAMIS accelerator¹⁸ at CSNSM with 1.2 MeV He, to determine Pb profiles. Such measurements also allowed us to check the Pb implanted fluence, which was systematically 30–40% higher than expected from ion current measurements during implantation, presumably due to sample charging effects. After implantation, samples were annealed in a quartz tube furnace at temperatures ranging from 800 to 900 $^{\circ}$ C for 1 h, under dry N $_2$ atmosphere, in order to minimize compositional changes in the glass during the anneal. Secondary ion mass spectrometry (SIMS) was performed with a Cameca IMS 4F probe at LPSC using a Cs $^+$ primary beam. Secondary ion signals were detected using an electron multiplier. The 30 Si signal was simultaneously recorded in order to determine the surface position and to correct for detector efficiency. Depth calibration was achieved by postanalysis crater depth measurements with a Tencor Stylus profilometer, assuming a constant sputtering rate. Transmission

electron microscopy (TEM) was performed on (1) the CSNSM Philips CM12 microscope operating at 120 keV in order to observe the nanocrystal phases, radii, and depth distribution according to a procedure described elsewhere,¹⁰ and (2) the CECM JEOL 2010 high-resolution electron microscope (HREM) equipped with a field emission gun operating at 200 kV for crystallographic structure identification. To compare the elemental depth distribution as deduced from SIMS with the element concentration in the nanocrystal distribution, we evaluated the latter by (i) determining the radius and depth of each nanocrystal in the TEM cross-sectional micrographs, (ii) in a given depth slice, summing the nanocrystal volumes (deduced from their radius), and (iii) dividing by the average TEM cross-section thickness and the number of molecules (in crystalline form) per unit volume (19.1 PbS \cdot nm $^{-3}$, 17.2 PbSe \cdot nm $^{-3}$, 14.9 PbTe \cdot nm $^{-3}$, 12.6 PbSO $_4$ \cdot nm $^{-3}$, 29.6 Te \cdot nm $^{-3}$). On a TEM micrograph, only a surface density of nanocrystals (i.e., surface concentration projected on the image plane along the direction of the electron beam) is measured. The thickness e of the cross-section sample, unless specified otherwise, was taken to be $e = 100$ nm (50–150 nm is a reasonable range of observable TEM sample thicknesses). As seen below (Figures 7–10), an error on the cross-section thickness may affect the agreement between the absolute quantities of elements as determined via TEM or SIMS, but it has no effect on the profiles and the profile modifications. Note that, in the following experiments, we used both TEM and photoluminescence to study the effect of reversing the (lead vs chalcogen) implantation sequence and found no significant differences. In the photoluminescence (PL) experiments conducted on (S + Pb) sequentially implanted samples (Section 6), an Ar laser operated at 488 nm was used for excitation; the sample's PL was collected by an optical fiber and dispersed by a Jobin Yvon TRIAX 320 spectrograph. The signal was detected by a PbS detector and corrected for the entire system collection efficiency using a tungsten lamp.

4. Results

Our previously reported SIMS measurements¹⁵ revealed definite discrepancies with the as-implanted concentration profiles expected from SRIM simulations. The Pb implanted profile was 20% larger and shifted to greater depths; on the other hand, S and Se distributions were closer to the surface than expected. Annealing in the range 850–900 $^{\circ}$ C/1 h led to clustering in all sequentially implanted samples, as shown below, and the postanneal nanocrystal depth distribution extended well beyond the initial concentration profiles. The evidence for (and consequences of) annealing-induced species diffusion are the main topic of this paper.

4.1. Phase Identification. The microstructure of all observed nanocrystal types was investigated by HRTEM. Several tens of precipitates were studied in each type of sample. Our results on Pb + S implanted silica, published elsewhere,¹² revealed growth not only of PbS (S in –II redox state) but also of PbSO $_4$ (S in +VI redox state) nanocrystals. In this case, a large fraction of the nanocrystals was polycrystalline, sometimes containing both the PbS and PbSO $_4$ phases (see Figure 1).

A similar structural behavior might have been expected in the case of Pb + Se implanted silica in view of the similarities between Se and S diffusion in silica. However, all observed lattice fringes spacings and zone axis (Figure 2) fully agreed with the standard $Fm\bar{3}m$ ($a = b = c = 6.13$ Å) cubic form of PbSe. Neither PbSeO $_3$ nor PbSeO $_4$ nanocrystals were observed. Moreover, only single crystals were found. To our knowledge, this is the first report of PbSe nanocrystal synthesis by sequential implantation in pure silica.

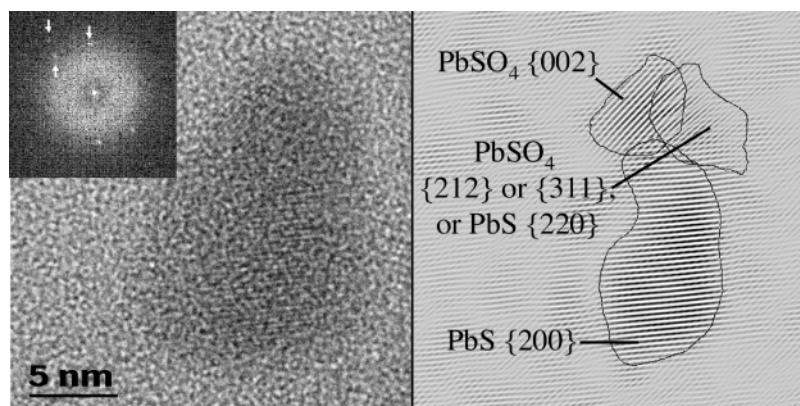


Figure 1. Example of polycrystalline PbS/PbSO₄ nanocrystal containing at least three domains differing by their interplanar distances and orientation. Inset: the FFT of the original image, showing three different couples of spots, indicating the presence of diffracting planes (arrow). In the FFT, one can filter the background so as to isolate the diffracting region corresponding to one particular couple of spots (filtered image on the left). See also ref 12.

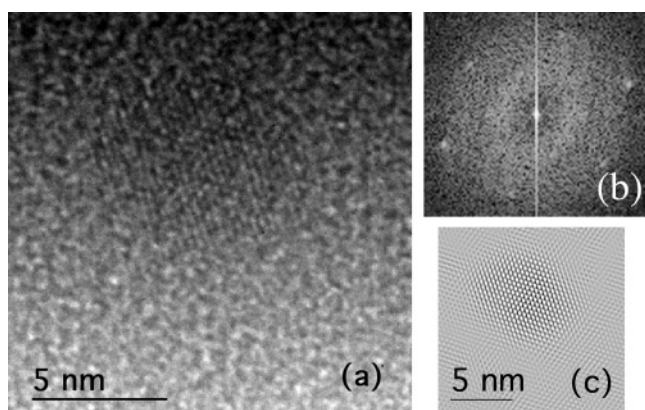


Figure 2. Zone axis [220] image of a cubic PbSe nanocrystal, showing two different interplanar distances $d_{200} = 3.06 \text{ \AA}$ and $d_{111} = 3.54 \text{ \AA}$ (a); FFT of the image, showing the symmetry of the zone axis (b); inverse FFT of the filtered FFT, so as to better isolate the nanocrystal lattice from the surrounding amorphous signal (c).

Structural identification in the case of Pb + Te sequentially implanted samples is not as straightforward. Almost all nanocrystals were monocrystalline (Figure 3), but phase identification by HRTEM was difficult because the interplanar distances of Te and PbTe are similar ($d^{\text{Te}}_{010} = 3.86 \text{ \AA}$ close to $d^{\text{PbTe}}_{111} = 3.73 \text{ \AA}$; $d^{\text{Te}}_{011} = d^{\text{PbTe}}_{200} = 3.23 \text{ \AA}$; $d^{\text{Te}}_{012} = 2.35 \text{ \AA}$ and $d^{\text{Te}}_{110} = 2.23 \text{ \AA}$ close to $d^{\text{PbTe}}_{220} = 2.28 \text{ \AA}$). All our measured interplanar distances were compatible with both phases. From the zone axis symmetry, two of the nanocrystals were identified as Te, but the orientation of the majority did not allow discrimination between PbTe and Te.

4.2. Phase Evolution during Annealing. In the earlier growth stages (as soon as a PL signal is observed (see Section 6), for example, after a 30 min anneal at 850 °C) we found rather large clusters (diameter $\approx 6 \text{ nm}$) identified as crystalline PbS or PbSe, surrounded by very small clusters whose diameter was below 2 nm, all localized inside the implantation profile. None of these small clusters exhibited lattice fringes under HRTEM. They were presumably amorphous, and their chemical composition could not be determined. Photoluminescence (PL) experiments on the corresponding PbS samples detected no signal at wavelengths below 1 μm for any of our annealing conditions (see below, Section 6), whereas, had these small nanocrystals been crystalline PbS, we should have expected light emission in this region, according to the size–gap relation for PbS nanocrystals.¹⁹ Our TEM experiments revealed that these clusters progressively dissolved as growth proceeded, contribut-

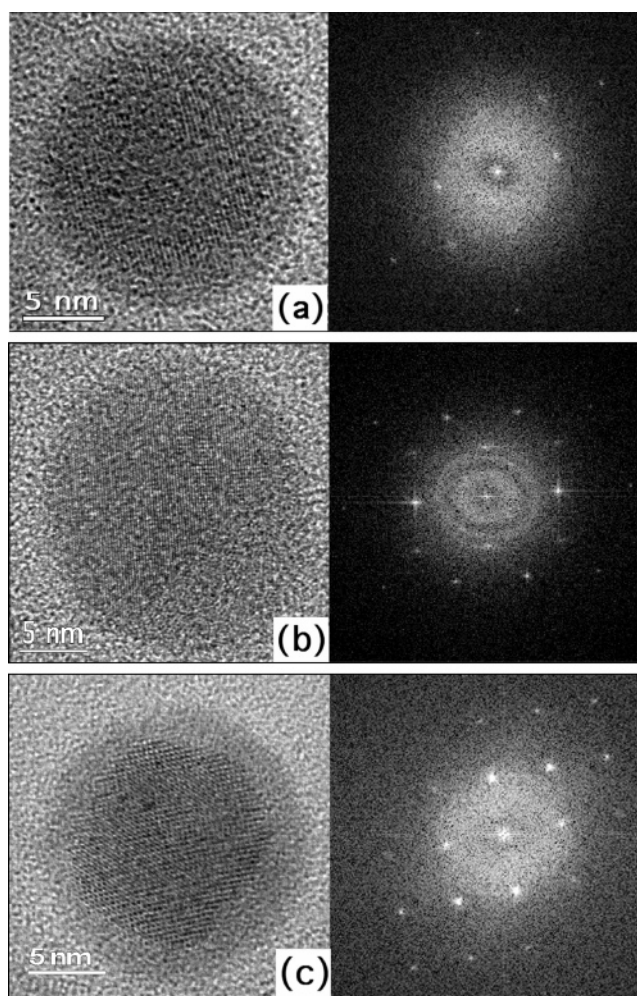


Figure 3. 3. PbTe [100] or Te zone axis (a) and (c). Te zone axis; the FFT of each image is on the right-hand side (b). In (c), the nanocrystal is probably melting under the electron beam.

ing to the growth of nearby PbS or PbSe nanocrystals (Figure 4a). Such nanocrystal growth, occurring via dissolution of preexisting amorphous clusters, is not at all typical of standard homogeneous nucleation. We suggest that it is due to the combination of chalcogen redox states in the case of PbS and PbSe (Figure 4b, see discussion in Section 5).

4.3. Postanneal Nanocrystal Depth Distribution: Influence of Chemistry. Sample annealing induced marked differences in the depth distributions of both the implanted constituents and

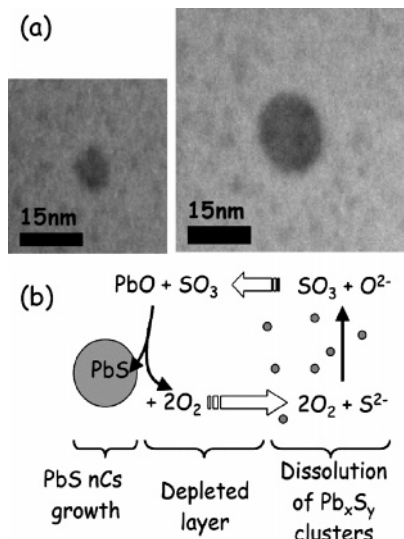


Figure 4. Pb + S sequentially implanted into silica after annealing at 850 °C/1 h. Examples of small amorphous precipitates in the depleted layer around large nanocrystals (a). Suggested mechanism of depleted layer formation (b).

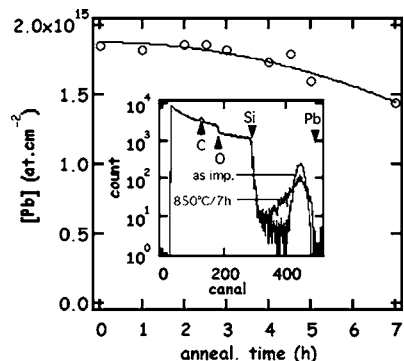


Figure 5. RBS measurement of Pb concentration ([Pb]) in S + Pb implanted sample with a 1.2-MeV He beam. Initial concentration was $1.88 \times 10^{15} \text{ Pb}\cdot\text{cm}^{-2}$ and decreased during annealing at 850 °C. Inset shows the RBS spectra for the as-implanted sample and after a 7 h anneal at 850 °C. Positions of the Pb, Si, O, and C surface peaks are indicated by an arrow (C was deposited before the RBS analysis so as to avoid sample charging during measurements).

the nanocrystals that they formed. RBS provided evidence (Figure 5) for very significant changes in the Pb concentration profile, even leading to a ~20% loss of Pb content from the samples after annealing up to temperatures corresponding to the nanocrystal formation range. These changes are a consequence of the differing chemical interaction of the chalcogens with SiO₂ or Pb. Figure 6 shows the nanocrystal density depth dependence as measured by TEM for each chalcogenide family. Nanocrystal growth of all three chalcogenides clearly occurs well outside of the as-implanted profiles:^{11,15} on the far side of the profile for Pb + S implanted samples, on both sides of the implanted region for Se + Pb, and again chiefly on the far side of the Te + Pb implanted region. An understanding of these results requires a study of each chalcogen's chemical interaction with the host and with Pb.

4.3.1. Precipitation in the S + Pb Implanted Sample. As noted above, a detailed SIMS analysis¹⁵ showed that our Pb and S profiles were somewhat shifted in opposite directions as compared to those expected from SRIM simulations; this accounts for the shift in Figure 6a between the maximum concentration (arrow) and the maximum nanocrystal density, but certainly not for the nucleation and growth of PbS and

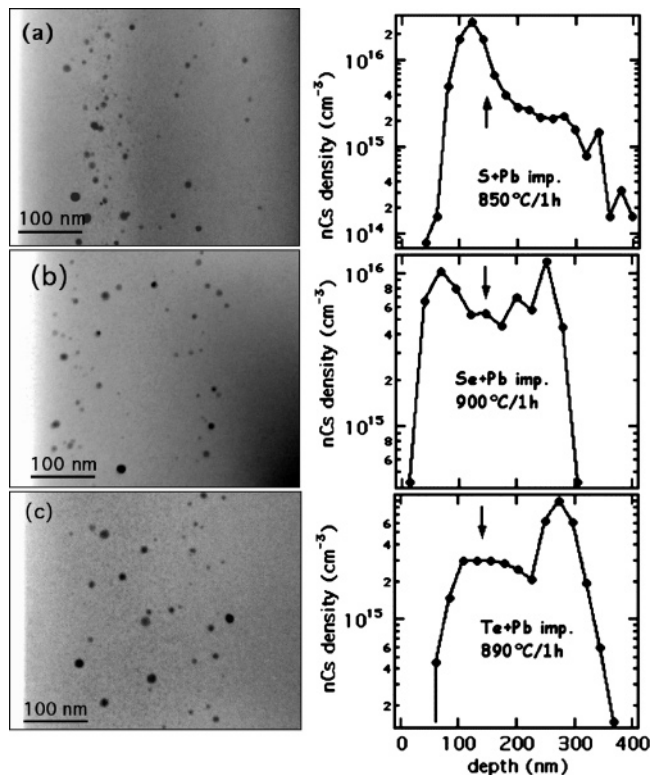


Figure 6. Left-hand side: Representative examples of TEM cross sections for different chalcogen implantation (SiO₂ surface is on left side of micrographs). S + Pb sequentially implanted silica; after annealing at 850 °C/1 h, nanocrystals grow on the low-depth side of the implanted profile (a). Se + Pb sequentially implanted silica; after annealing at 900 °C/1 h, nanocrystals grow on both outer sides of the implanted profile (b). Te + Pb sequentially implanted silica; after annealing at 900 °C/1 h, nanocrystals grow within and on the high-depth side of the implanted profile (c). Right-hand side: Measured density of nanocrystals in the same samples, determined by TEM. The arrow indicates the position of the initial Pb and chalcogen concentration maximum (Table 1): $R_p(\text{Pb}) = 144 \text{ nm}$; $R_p(\text{S}) = 136 \text{ nm}$; $R_p(\text{Se}) = 141 \text{ nm}$; $R_p(\text{Te}) = 140 \text{ nm}$.

PbSO₄ nanocrystals outside of the implanted profile. In refs 11 and 15, the Pb and S concentration profiles were determined independently after annealing of a sample implanted with only one of the elements. But in the sequentially implanted samples, the mobility of a species is affected both by its interaction with the other and by the occurrence of precipitation. Hence, we measured both the Pb and S concentration profiles in the *sequentially implanted* sample after annealing (Figure 7a), and checked that, as detailed in ref 15, the total amount of precipitated PbS (or PbSO₄) at a given depth is controlled by the least concentrated element. The fast-diffusing oxidized form of sulfur determines the depth distribution of PbS and/or PbSO₄ nanocrystals, leading to precipitation outside of the implanted profile.

We were unable to determine whether PbSO₄ is the main precipitated phase in the in-depth region ($z > 250 \text{ nm}$) of the sample. However, we observed both the PbS and PbSO₄ phases in a sample annealed 4 h at 900 °C, for which 70% of the nanocrystals had grown outside the implanted profile (Figure 7b). In most cases, we could not distinguish between the PbS and PbSO₄ structures; however, of the 12 precipitates whose structure was identified, five contained both the PbS and PbSO₄ phases and seven were PbSO₄. This suggests that equilibrium was reached between both sulfur redox states after sufficient annealing, facilitated by fast-diffusing SO₃ (see reaction 1, Section 5).

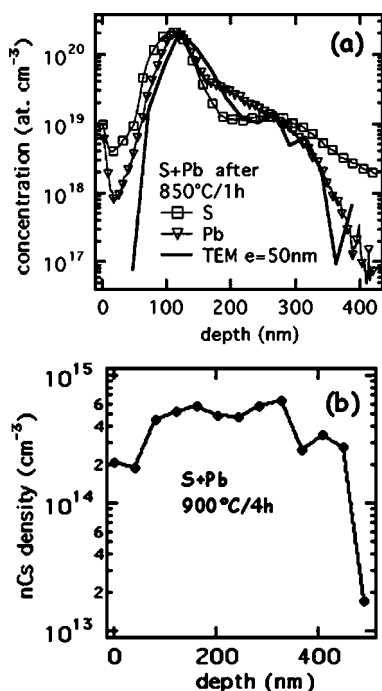


Figure 7. Total concentration profiles of Pb and S compared to the nanocrystal depth distribution measured by TEM (a). Sample thickness was taken as $e = 50$ nm so as to match SIMS concentration and TEM measurement. All samples were annealed 1 h at 850 °C. Precipitation is governed by the least-concentrated element. Nanocrystal density depth distribution in the same class of sample after annealing 4 h at 900 °C (b). More than 70% of the nanocrystals have grown outside of the initial ($70 < z < 200$ nm) implanted profile.

4.3.2. Comparison Between PbSe and PbS. Chalcogen diffusion experiments¹¹ showed that S and Se are chemically very similar as opposed to Te; when implanted into SiO₂, they both have two different oxidation states, one of which is quasi-immobile, whereas the other is very mobile. However, the oxidized form of selenium is likely the +IV state (versus +VI for sulfur), which is less mobile. In our Se + Pb sequentially implanted samples, the Se implantation energy and fluence were chosen so that the depth and concentration were identical to those of S in the S + Pb sequentially implanted samples of Table 1. But in this case, TEM experiments (Figure 6b) show that nanocrystals are preferentially synthesized on either side of (rather than inside) the implanted profile, in strong contrast to the (S + Pb) implanted sample, and SIMS profiling confirms that this is due to Pb and Se transport (Figure 8a). Moreover, the PbSe nanocrystals' average radii (Figure 8b) are larger on both sides of the implanted profile than in its center. Our results indicate that, although they are only a small fraction of the total, the mobile oxidized chalcogens play a major role in promoting nucleation and growth outside the implanted profile. Also, a comparison of the (S + Pb) and (Se + Pb) results clearly shows that the chemical interactions of chalcogens with both the host and the sequentially implanted Pb affect the depth at which nucleation and growth occur.

4.3.3. The Special Case of PbTe/Te. Nucleation and growth outside of the implanted profile was also observed after (Te + Pb) sequential implantation and annealing (Figure 6c). In Figure 9, we compare the initial concentration profile as determined by SRIM with the elements' concentration profile in precipitated form as measured by TEM. Because, as noted above, Te and PbTe precipitates could not be distinguished, the precipitated concentration was plotted, assuming 100% of one or the other. Approximately half of the precipitated concentration is outside

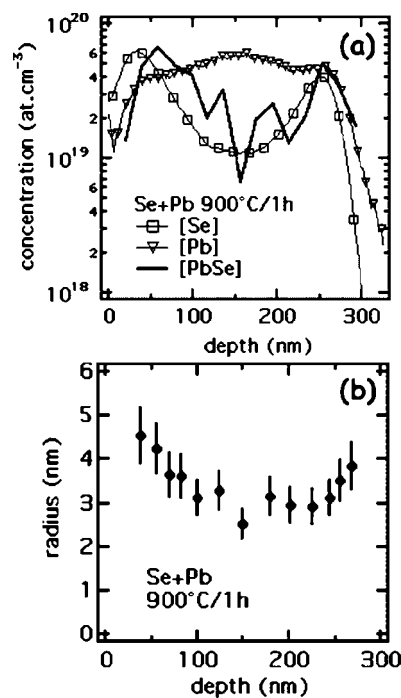


Figure 8. Growth characteristics of the sample annealed 1 h at 900 °C after Se + Pb sequential implantation in pure silica. Total concentration profiles of Pb (triangle) and Se (square) as measured by SIMS compared to those deduced from TEM via PbSe nanocrystals distribution (thick line) (a). The precipitated amount is governed by the least concentrated element. Depth dependence of PbSe nanocrystal radii (b). Each point is an average over 49 precipitates, its abscissa being the average depth and the ordinate their average radius. Error bars are statistical because of the finite averaging ensemble size.

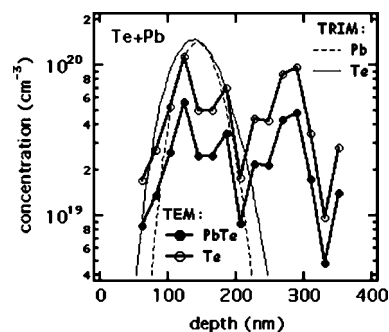


Figure 9. Comparison of initial concentration profiles of Pb and Te as determined by SRIM (Table 1) with the precipitated element concentration, as deduced from TEM under the assumption that *all* precipitates are either PbTe (full circles) or Te (empty circles). The sample is (Te + Pb) sequentially implanted silica annealed 1 h at 890 °C.

of the implanted profile. As we identified no very mobile form of Te in diffusion experiments, and because, contrary to the cases of S and Se,¹¹ no Te was found outside of the implantation profile when implanting the sample with Te alone and annealing under the same conditions, we cannot ascribe nucleation and growth outside of the implanted profile to diffusion. We suggest that the presence of Pb provides a chemical interaction that enhances Te mobility, leading to precipitation outside the implanted profile.

The Pb–chalcogen chemical interaction and its effect on the diffusion properties and precipitation can be evidenced by comparing the postanneal profile of the elements in SiO₂ when implanted alone or sequentially implanted. Figure 10a shows the effect on the sulfur concentration profile of identical anneals (1 h at 900 °C) for a S (or Pb) implanted sample versus a (S +

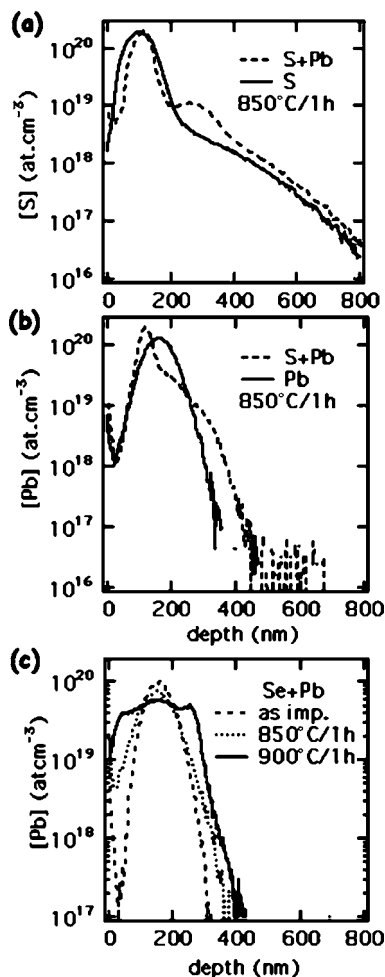


Figure 10. Modification of implanted atom mobility by the Pb-chalcogen interaction (from SIMS measurements). Comparison of S concentration after a 1 h anneal at 850 °C of S implanted and S + Pb implanted silica (a); comparison of Pb concentration after a 1 h anneal at 850 °C of Pb implanted and S + Pb implanted silica (b). Pb concentration in the Se + Pb sequentially implanted silica, after annealing at different temperatures (c). The difference between (b) and (c) illustrates the chalcogen's influence on Pb mobility.

Pb) implanted sample. In the latter case, while precipitation within the implanted profile leads to a decrease of the profile width, a well-known effect,²⁰ there is significant sulfur in-depth profile broadening due to precipitation with Pb. The latter element's profile is also broadened, its mobility being enhanced by its interaction with fast-moving sulfur (Figure 10b). In the case of the (Se + Pb) sample, a similar effect occurs (Figure 10c), except that nanocrystal formation now occurs on both slopes of the implanted profile rather on one side. The difference in chemical behavior of Se and S relative to Pb is presumably the source of this effect.

5. Discussion

5.1. Effect of Redox Properties on Nucleation. We have shown that chalcogenide nanocrystal formation in these sequentially implanted samples cannot be analyzed in simple nucleation theory terms. We discuss a possible mechanism for nanocrystal nucleation and growth that takes the known chemical properties into account and involves intermediate steps.

Upon annealing, slow-diffusing Pb combines with the reduced form of the chalcogen inside the implantation profile to form the small amorphous clusters identified in our (S + Pb) samples. The small, oxidized (e.g., SO₃ or SeO₂) chalcogen fraction is

likely a key factor of growth due to its much faster diffusion.¹¹ Growth of PbS and/or PbSO₄ then occurs by the two reactions:



The oxygen freed in these reactions diffuses inside the implanted profile, contributing to the dissolution of amorphous Pb polysulfide clusters, leading to PbO and to mobile SO₃ groups (e.g., via the reaction $\text{S}^{2-} + 2\text{O}_2 \rightarrow \text{SO}_3 + \text{O}^{2-}_{\text{glass}}$) so that, in turn, reactions 1 and 2 again promote PbS nanocrystal nucleation and growth. The process is summarized in Figure 4b. Nanocrystal synthesis may thus occur via different nucleation paths: (i) the reaction of free Pb with diffusing SO₃, leading to either PbSO₄ or directly to PbS, (ii) the reduction of PbSO₄ nanocrystals, (iii) the crystallization of small precursors Pb_xS_y (with the help of SO₃?), and possibly, (iv) the reaction of free lead with S²⁻. Analogous nucleation stages may be operative in the case of PbSe because of the chemical similarity between S and Se. For PbTe, whose chemistry differs markedly, nucleation mechanisms should also differ, but at least two distinct nucleation paths are possible: (i) direct formation of PbTe nanocrystals by the reaction of isolated Pb and Te or (ii) initial formation of Te nanocrystals (much less soluble in silica than Pb) and incorporation of Pb as annealing proceeds. Finally, and most importantly, the high diffusivity of the sulfate (or, to a lesser extent, sulfite) groups could explain why PbS nanocrystal growth tends to occur on the slopes of the implanted profiles (see below).

5.2. On Nucleation and Growth Outside of the Implanted Profile. According to classical nucleation and growth theory for an AB mixture,^{21,22} precipitation outside of the implanted profile should not occur. From the Gibbs–Thompson relation, the solubility of B at the surface of stable nanocrystals (with radius $R > R^*$) is lower than that of B at the surface of a nanocrystal with a critical radius R^* at the stability threshold. If precipitates have already reached the coarsening stage inside an implanted profile, the mean concentration of B in the A-rich phase is close to its solubility value at the average-size nanocrystal's surface. Were this picture valid in our systems, outdiffusion from the precipitate region should only lead to average concentrations below the stable nucleus formation limit. Nucleation and growth might then occur in pre-coarsening growth stages, but not once the majority of B has precipitated. This is in strong contrast to our observations. In the case of sequentially implanted (S + Pb) samples, for example, combined SIMS and TEM experiments show that essentially all the Pb and S are contained in a PbS + PbSO₄ nanocrystal profile after a 1 h anneal at 850 °C (Figure 7a), a profile that broadens continuously as annealing proceeds to higher temperatures and longer times (Figure 7b).¹⁰ Clearly, our sequentially implanted systems do not satisfy the criteria of classical theory.

In fact, of course, our samples are far from the binary mixture situation referred to above because three elements (the chalcogen, Pb and O) and their compounds are involved in growth. Kuehman and Voorhees²³ found that, in a ternary system in which coarsening involves three simultaneous Gibbs–Thompson relations, each of these depend on all diffusion coefficients and solubilities in the various constituent nanocrystal phases. Moreover, the compositional ratio varies greatly in our samples. For example, in the (S + Pb) sample annealed 1 h at 850 °C (Figure 7a), PbS and PbSO₄ nanocrystals are formed both in a Pb-excess region (at depths between 120 and 270) nm and in a S-excess region (depths below 120 nm or beyond 270 nm). In

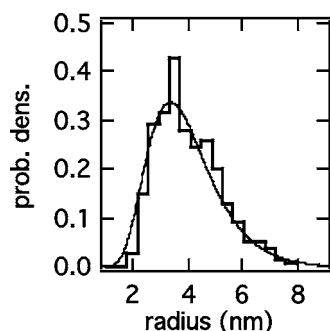


Figure 11. Example of size distribution in S + Pb implanted sample after annealing at 850 °C/1 h (400 precipitates). The thin line is the adjustment by a log-normal probability density function $f_{\log\text{-normal}}(R = r) = 1/(r \ln(\sigma)\sqrt{2\pi}) \exp(-(\ln(r/\mu))^2/2(\ln(\sigma))^2)$ with $\mu = 3.7$ nm and $\sigma = 1.4$.

the Se + Pb sample annealed at 900 °C/1 h (Figure 8), PbSe nanocrystals are formed both in a Pb-excess region (beyond 50 nm) and in a Se-excess region (below 50 nm); at the projected range of Se and Pb, the uncombined Pb concentration is at least 2–3 times larger than that contained in PbSe nanocrystals.

Redox chemistry, such as eqs 1 and 2, must be involved in the growth process, including the various redox states of the chalcogen and of all possible O states, such as 0 for O₂, or -II for O²⁻_{glass}, SeO₂, and PbO. A quantitative approach to the results should account not only for thermodynamical features (the equilibrium concentration of the oxidized forms, the chemical interaction between the oxidized and the reduced forms, the magnitude of the chemical interaction of each chalcogen with Pb), but also for the nucleation and growth kinetics (the diffusion of the oxidized form of Se being slower than that of S, the dissolution kinetics of small amorphous clusters formed inside the implantation profile, the dominating nucleation mechanism in the Se + Pb case...). This is clearly a very ambitious program for the future.

5.3. Nanocrystal Size Distributions. The present work was undertaken in an attempt to produce a high density of small nanocrystals for optical applications. Control over the average nanocrystal size and narrowness of the size distribution are thus a crucial feature. Our TEM pictures (Figure 6) show that, despite the differences described above in the diffusion coefficients and chemical state of chalcogens, the final average nanocrystal radii in our annealed samples were all quite similar ($\langle R \rangle_{\text{PbS}} = 2.8$ nm, $\langle R \rangle_{\text{PbSe}} = 3.45$ nm, $\langle R \rangle_{\text{PbTe or Te}} = 4.05$ nm), as were the size distributions. The latter are asymmetric, as shown in Figure 11, and approach a log-normal shape whose geometrical standard deviation is systematically about 1.45. A discussion of these features, on the basis of work²⁴ performed in various areas of growth science, is given in ref 10, which shows that their very existence testifies to the absence of any precise information on the growth process. Multiple nucleation and growth processes occur, as listed in the preceding paragraphs; their interference blurs the effect that each alone would have on the size distribution. This memory loss translates to a fast relaxation of the size distribution to its asymptotic log-normal shape. This interpretation is supported by the fact that, in the annealed (S + Pb) and (Se + Pb) samples, identical log-normal size distributions were found at different depths, i.e., whether the nanocrystals had grown inside or (after diffusing) outside of the initial implantation profile.

6. Optical Emission Properties

The limited implantation depth (typically 100–200 nm) and fluence do not produce a sufficient number of nanocrystals to

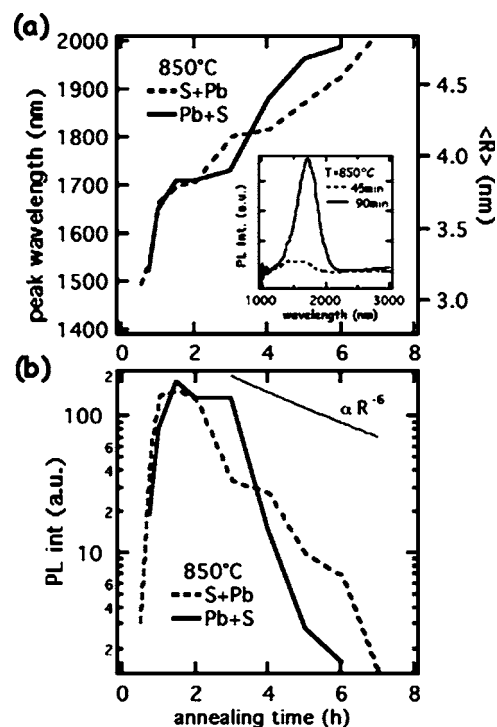


Figure 12. PL emission properties of S + Pb and Pb + S sequentially implanted sample as a function of annealing time at 850 °C/1 h. Increase of the peak wavelength maximum, the inset being examples of PL spectra (a). On the right side of the graph is the mean radius, corresponding to the peak wavelength, estimated by the model in ref 19. PL intensity variations (b). The thin line is proportional to R^{-6} as estimated with the help of data in (a).

observe optical absorption in our samples, but a rather intense PL due to the first exciton state was observed¹² in the (S + Pb) implanted samples, and more results of this system are discussed below. On the other hand, the (Se + Pb) sequentially implanted samples failed to display any PL despite TEM evidence for the presence of PbSe nanocrystals with a radius below 7 nm after annealing (Figures 6b and 8b). Assuming, for simplicity, a gap $E_g = 0.28$ eV, as deduced from the nanocrystal size-gap relation,¹⁹ and an effective mass $m^* = 0.077 m_e$, such nanocrystals should have emitted light at wavelengths below about 3 μm (which was the spectral detection limit of our PbS detector). The absence of any signal was possibly due to PL quenching by very efficient photoexcited carriers or to surface defect-induced nonradiative transitions. Why this should affect PbSe and not PbS remains unclear.

The (S + Pb) samples exhibited significant PL as soon as nanocrystal growth set in. Figure 12a shows the PL of a sequentially implanted sample annealed at 850 °C for different durations. The PL signal was centered at about 1.5 μm (fwhm = 0.5 μm) after a 30 min anneal. As the annealing time increased, the PL line intensity increased considerably and displayed a red-shift (centered at 1.6–2.0 μm after a 2–3 h anneal) due to nanocrystal growth. Further annealing led to a decrease in the PL intensity, which disappeared after an 8 h anneal (Figure 12b). The nanocrystal radius, deduced from the PL intensity maximum via ref 19 (right-hand side of Figure 12a), may be compared to the values measured via TEM after several anneals. For example, after a 1 h anneal at 850 °C, we find $\langle R \rangle = 3.8$ nm from TEM, corresponding to a lowest exciton state emission wavelength at 1.6 μm , according to the model. Other experimental TEM determinations of mean nanocrystal radii for longer anneals ($\langle R \rangle$ (900 °C/1 h) = 4.1 nm, $\langle R \rangle$ (900 °C/2 h) = 4.5 nm, and $\langle R \rangle$ (900 °C/4 h) = 5.1 nm) also compare

favorably with values deduced from PL experiments in Figure 12a. We note that such estimates are only indicative, the model in ref 19 being valid for perfectly spherical nanocrystals with infinite confinement barriers, whereas our microstructures include polycrystalline nanocrystals and PbSO₄/PbS interfaces. Also, and importantly, our comparison concerns the average nanocrystal sizes, whereas the rather broad observed PL emission line presumably involves contributions from nanocrystals of different sizes. But the correlation between the average PL peak wavelength shift and nanocrystal size is a reasonable indication that the observed PL is due to the confined exciton within the PbS nanocrystals, and the relation between PbS nanocrystal sizes, average PL emission wavelength, and PL intensity provides additional information on the growth mechanisms. For example, the PL intensity increase with annealing time was very sharp, whereas the PL position remained fairly constant. This is consistent with TEM observations (Figure 4a), showing that growing nanocrystals very rapidly reach a mean radius of about 3–3.5 nm at the expense of smaller amorphous (hence nonemitting) clusters.

Regarding the sharp PL intensity decrease after a 2 h anneal at 850 °C (Figure 12b), we note the following. The PL intensity I_{PL} scales as $n \cdot f_{\text{osc}}$ where n is the PbS nanocrystal density and f_{osc} , their oscillator strength. Predictions based on the electron and hole wave function overlap, leading to $f_{\text{osc}} \propto R^{-3}$ for a crystallite with radius R .²⁵ Assuming that the PbS nanocrystal volume fraction is conserved in our system, increasing the average nanocrystal size leads to a density decrease varying as $n \propto R^{-3}$ and, hence, to the $I_{\text{PL}} \propto R^{-6}$ dependence shown as a thin line in Figure 12b. In fact, the experimental PL intensity decreased much more rapidly. This discrepancy may be due to several causes: a PbS nanocrystal volume fraction decrease by outdiffusion from the sample during long anneals (Figure 5), a partial reverse transformation of PbS into PbSO₄, and/or the increasing influence of nonradiative paths as annealing proceeds.

7. Conclusion

We have synthesized lead chalcogenide nanocrystals by sequential implantation of the components into pure silica. The redox properties of the nanocrystal constituents, especially those of the chalcogens, are shown to have a major influence on the nanocrystal microstructures as well as on their growth characteristics, final size distribution, and spatial repartition. We have shown that the use of ion implantation as a means of synthesis cannot bypass these redox properties because the required postannealing process activates the chemical interactions of the implanted elements among themselves and with the host. As a result, it is impossible to rely on the initial implantation profiles to predict the nanocrystals' depth distribution; the coupling between diffusion and precipitation must be taken into account. The rather complex chalcogen chemistry also leads to multiple nucleation mechanisms, possible transient nanocrystal chemical compositions, and differing final nanocrystal compositions for

different chalcogens (e.g., PbS and PbSe versus pure Te). Its effect on diffusion leads to lack of growth control and affects the size distribution broadening. Controlling the redox chemistry (chemical nature of the matrix, composition of the annealing atmosphere) is a prerequisite to reaching better control over growth and, hence, over the lead chalcogenide optical properties. In the case of PbS, we have succeeded in obtaining intense, although rather broad, optical emission in the range 1.5–2.0 μm .

References and Notes

- (1) Borelli, N. F.; Smith, D. W. *J. Non-Cryst. Solids* **1994**, *180*, 25.
- (2) Lipovskii, A. A.; Kolobkova, E. V.; Petrikov, V. D. *Proc. SPIE-Int. Soc. Opt. Eng.* **1997**, *2967*, 30.
- (3) Lipovskii, A.; Kolobkova, E.; Petrikov, V.; Kang, I.; Olkhovets, A.; Krauss, T.; Thomas, M.; Silcox, J.; Wise, F.; Shen, Q.; Kycia, S. *Appl. Phys. Lett.* **1997**, *71*, 3406.
- (4) Craievich, A. F.; Alves, O. L.; Barbosa, L. C. *J. Appl. Crystallogr.* **1997**, *30*, 623.
- (5) Craievich, A. F.; Kellermann, G.; Barbosa, L. C.; Alves, O. L. *Phys. Rev. Lett.* **2002**, *89*, 235503.
- (6) Meldrum, A.; Withrow, S. P.; Zuhr, R. A.; White, C. W.; Boatner, L. A.; Budai, J. D.; Anderson, I. M.; Henderson, D. O.; Wu, M.; Ueda, A.; Mu, R. *Microcryst. Nanocryst. Semicond. 1998, Symp.* **1998**, *536*, 317.
- (7) Meldrum, A.; Sonder, E.; Zuhr, R. A.; Anderson, I. M.; Budai, J. D.; White, C. W.; Boatner, L. A.; Henderson, D. O. *J. Mater. Res.* **1999**, *14*, 4489.
- (8) White, C. W.; Budai, J. D.; Meldrum, A. L.; Withrow, S. P.; Zuhr, R. A.; Sonder, E.; Purezky, A.; Geohagan, D. B.; Zhu, J. G.; Henderson, D. O. *Atomistic Mechanisms in Beam Synthesis and Irradiation of Materials*; Materials Research Society: Warrendale, PA, 1999; p 399.
- (9) Meldrum, A.; White, C. W.; Boatner, L. A.; Anderson, I. M.; Zuhr, R. A.; Sonder, E.; Budai, J. D.; Henderson, D. O. *Nucl. Instrum. Methods Phys. Res., Sect. B* **1999**, *148*, 957.
- (10) Espiau de Lamaestre, R. Ph.D. Thesis, University Paris XI, 2005; Espiau de Lamaestre, R.; Bernas, H. To be published.
- (11) Espiau de Lamaestre, R.; Jomard, F.; Majimel, J.; Bernas, H. *J. Non-Cryst. Solids*, **2005**, *351*, 3031.
- (12) Espiau de Lamaestre, R.; Bernas, H.; Ricolleau, Ch.; Majimel, J. IBMM2004, *Nucl. Instrum. Methods Phys. Res. Sect. B*, submitted for publication.
- (13) Volf, M. B. *Chemical Approach to Glass*; Elsevier Science Publishing Company Inc.: New York, 1984; S: p 524; Se: p 544; Te: p 554.
- (14) Shelby, J. E. *Handbook of Gas Diffusion in Solids and Melts*; ASM International: Materials Park, OH, 1996; p 191.
- (15) Espiau de Lamaestre, R.; Bernas, H.; Jomard, F. *Nucl. Instrum. Methods Phys. Res., Sect. B* **2004**, *216*, 402.
- (16) Chaumont, J.; Lalu, F.; Salome, M.; Lamoise, A. M.; Bernas, H. *Nucl. Instrum. Methods Phys. Res.* **1981**, *189*, 193.
- (17) Ziegler, J. F.; Biersack, J. P.; Littmark, U. *The Stopping and Range of Ions in Solids*; Pergamon Press: New York, 1985.
- (18) Bernas, H.; Chaumont, J.; Cottureau, E.; Meunier, R.; Traverse, A.; Clerc, C.; Kaitasov, O.; Lalu, F.; Ledu, D.; Moroy, G.; Salomé, M. *Nucl. Instrum. Methods Phys. Res., Sect. B* **1992**, *62*, 416.
- (19) Wang, Y.; Herron, N. *J. Chem. Phys.* **1991**, *95*, 525.
- (20) Trinkaus, H.; Mantl, S. *Nucl. Instrum. Methods Phys. Res., Sect. B* **1993**, *80/81*, 862.
- (21) Porter, D. A.; Easterling, K. *Phase Transformations in Metals and Alloys*; Chappman and Hall: London, 1992.
- (22) Haasen, P. *Physical Metallurgy*; Cambridge University Press: New York, 1996.
- (23) Kuehmann, C. J.; Voorhees, P. W. *Metall. Mater. Trans. A* **1996**, *27*, 937.
- (24) Limpert, E.; Stahel, W. A.; Abbt, M. *Biosci.* **2001**, *51*, 341–352.
- (25) Kayanuma, Y. *Phys. Rev. B* **1988**, *38*, 9797.

PbS nanocrystal synthesis in Pb-containing silicate glasses

R. Espiau de Lamaëstre

*Centre de Spectrométrie Nucléaire et de Spectrométrie de Masse, Unité Mixte de Recherche (UMR) 8609
Centre National de la Recherche Scientifique (CNRS), Université Paris Sud, 91405 Orsay Campus,
France and Fontainebleau Research Center, Corning, 77210 Avon, France*

H. Bernas^{a)}

*Centre de Spectrométrie Nucléaire et de Spectrométrie de Masse, Unité Mixte de Recherche (UMR) 8609
Centre National de la Recherche Scientifique (CNRS), Université Paris Sud,
91405 Orsay Campus, France*

(Received 12 May 2005; accepted 7 October 2005; published online 30 November 2005)

We describe a synthesis of PbS nanocrystals in glasses, involving 150 keV sulfur implantation into Pb-containing silicate glasses at peak concentrations up to 3.6 at. % and postannealing around the glass transition temperature (500–600 °C). The PbS nanocrystals, whose growth is evidenced by transmission electron microscopy, display intense photoluminescence (PL) in the 1–1.5 μm wavelength range. Besides bypassing the sulfur retention problem occurring in traditional glass fusion techniques, our method improves control over nucleation and growth. The latter is demonstrated by the impact on the PbS nanocrystal PL properties of progressively replacing CaO by ZnO in a S-implanted Pb glass. © 2005 American Institute of Physics. [DOI: 10.1063/1.2132091]

I. INTRODUCTION

Synthesizing semiconductor nanocrystals in glasses is of considerable interest for photonic applications since the quantum confinement of photon- or electron-induced carriers gives rise to several remarkable optical properties. For example, quantum-dot-doped materials may be used as gain media for lasers.^{1,2} The fast nonlinear absorption of PbS-doped glasses makes them candidates for use as saturable absorbers.^{3,4} Moreover, in the case of PbS, its low bulk band-gap energy ($E_g=0.41$ eV) and small effective mass ($m^*=0.12m_0$) combine to allow wavelength tuning in a broad range: an effective band gap around 1.5 μm is obtained for average nanocrystal radii around 3 nm (strong confinement regime).

The control of semiconductor nanocrystal nucleation and growth in glasses poses a number of basic problems, however. These are related to the complex thermodynamics of such multicomponent systems, e.g., their diffusion properties and phase diagrams are strongly affected by multiple charge state and defect interactions. Traditional preparation methods consist in introducing the nanocrystal components directly into the glass melt. After pouring and cooling, the glass may be heated to promote more or less controlled nanocrystal growth. This method has been successfully applied to the synthesis of PbS in silicate glasses.⁵ Fine adjustment of the glass composition is compulsory to obtain adequate sulfur retention during glass melting and is also important (although rarely mentioned) for nucleation and growth control during subsequent annealing. Rather low maximum chalcogenide concentrations were obtained in this way: about 0.1 at. % in borosilicate glasses^{6–9} and below 1 at. % in phosphate glasses.^{10,11} Ion implantation is apparently an at-

tractive solution to the problem of sulfur retention, as the implants' depth and concentration may be controlled via the implantation energy and fluence. PbS nanocrystal synthesis was reported by high-dose ($2.5\text{--}7.5 \times 10^{16}$ at. cm^{-2}) implantation of both Pb and S into pure silica followed by annealing at 1000 °C.^{12–15} However, growth control turns out to be poorer than by using the fusion method, and even control over the depth dependence of nanocrystal growth is lost.^{13,16} We have shown elsewhere that the use of ion implantation in pure silica cannot circumvent the quite complex chemical interactions of chalcogen elements with both Pb and the glass host.^{17,18} In the work presented here, we have implemented an alternate solution to PbS nanocrystal synthesis by combining a nonequilibrium technique (ion implantation of S) with adequate control over the chemical properties of Pb-containing soda-lime glasses.

Controlling PbS nanocrystal synthesis in silicate glasses simultaneously requires a means of introducing a significant amount of sulfur while adjusting the glass composition so as to control the precipitation chemistry. We show that both of these constraints may be satisfied independently by sulfur ion implantation into appropriate Pb-containing silicate glasses. We demonstrate that rather high PbS nanocrystal concentrations may be obtained by this hybrid method. We then extend it to a wider range of glass compositions, facilitating control of PbS nanocrystal growth. An example involves the progressive replacement of CaO by ZnO in a Pb-containing soda-lime silicate glass.

II. EXPERIMENT

Glasses were prepared at the Corning Research Center by adding lead oxide to a silicate base glass: the components were mixed in silica crucibles before melting at 1550 °C for 3 h *in air*. After pouring, glasses were annealed for 1 h at 580 °C and cooled slowly to avoid strain. Table I shows the

^{a)}Author to whom correspondence should be addressed; FAX: +33 16915 5268; electronic mail: bernas@cnsnm.in2p3.fr

TABLE I. Lead-glass composition and glass transition temperature T_g (DTA curve onset) of the samples studied in this work and corresponding sulfur implantation fluences (the implantation energy was 150 keV). The total (ZnO+CaO) composition was always 8.5 mol %.

mol %	Pb3	ZnPb0	ZnPb1	ZnPb5	ZnPb9
SiO ₂	64	74	74	74	74
Na ₂ O	15.5	16	16	16	16
CaO	10.5	8.5	7	3.5	0
ZnO	0	0	1.5	5	8.5
PbO	10	1.5	1.5	1.5	1.5
T_g (°C)	495	535	530	515	515
Pb (at. %)	3.6	0.5	0.5	0.5	0.5
Fluence (at. cm ⁻²)	3.4×10^{16}	4.7×10^{15}	4.7×10^{15}	4.7×10^{15}	4.7×10^{15}

batch compositions used in this work. The glass referenced Pb3 (resp. PbZn) contains 3.6 at. % (resp. 0.5 at. %) Pb, i.e., an order of magnitude above the upper limit (<1 wt. % SO₃ leading to 0.3 at. % S) reached^{19,20} by melting the same glass in a SO₃ atmosphere. Their glass transition temperatures T_g are in the range of 500–540 °C. Sulfur was added to the glass by ion implantation using the IRMA (Ref. 21) facility at Orsay. Sulfur ions were implanted at 150 keV at fluences (Table I) such that the maximum S concentration was equal [according to stopping and range of ions in matter (SRIM) simulations]²² to that of Pb. Samples were postannealed in a quartz tube furnace under dry N₂ atmosphere at temperatures close to T_g . Precipitated phases were monitored via transmission electron microscopy (TEM) with a Philips CM12 microscope operated at 120 kV. Continuous-wave (cw) photoluminescence (PL) spectra, obtained at room temperature with a InGaAs detector, also allowed monitoring of the nanocrystal growth from knowledge of the size-wavelength relation.²³

III. RESULTS AND DISCUSSION

A. PbS nanocrystal growth from a S-implanted lead glass

The TEM observation of our S-implanted Pb3 glass annealed for 1 h at 570 °C clearly shows (Fig. 1) the growth of PbS nanocrystals (average radius of 3–4 nm around the implanted sulfur depth distribution maximum, ca. 150 nm). As-

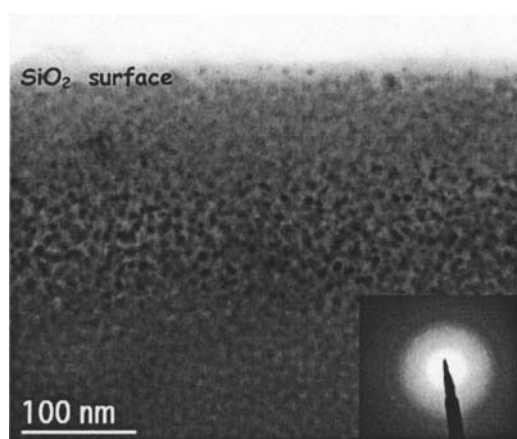


FIG. 1. TEM micrograph of S-implanted Pb3 glass after a 1 h anneal at 570 °C. Inset: selective area electron diffraction showing diffraction spots and narrow rings due to PbS nanocrystals.

suming that the entirety of implanted sulfur has precipitated into 3.5 nm radius nanocrystals, the average nanocrystal density within the implanted layer would be 2×10^{18} cm⁻³ (i.e., 2×10^{13} /implanted cm²). The nanocrystal density on the TEM micrograph (Fig. 1) is compatible with this figure. PbSO₄ precipitates, which were found previously²⁴ after (Pb+S) coimplantation into pure silica, are absent due to the use of a glass of higher basicity (soda-lime silicate instead of pure silica), favoring the reduced sulfur form S(-II) at the expense of the oxidized form S(+VI).^{19,20,25} Nucleation outside of the implanted profile is limited; measurements of the sulfur diffusion profile by secondary ion mass spectrometry (not shown here) of a S-implanted silicate glass (74 mol % SiO₂, 16 mol % Na₂O, and 10 mol % CaO) annealed at temperatures up to 100 °C above T_g exhibit no diffusion tail, as opposed to those observed in similar experiments with a pure silica host.²⁶ In the latter, the diffusion tail was ascribed to the very mobile oxidized sulfur S(+VI), whose concentration must be far lower in the base silicate glass used here.

B. Photoluminescence

The PL spectrum of the sample shown in Fig. 2 peaks at a wavelength of 1.56 μm. According to Wang and Herron,²³ this corresponds to the effective gap of a 3.5 nm radius PbS

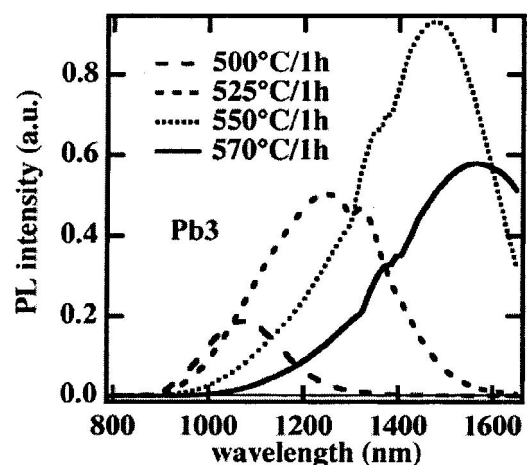


FIG. 2. PL spectra of the S-implanted Pb3 glass after a 1 h anneal at different temperatures. The PL intensity is maximized at temperatures close to T_g . The maximum PL shifts towards longer wavelengths as the annealing temperature is increased, i.e., as growth proceeds.

nanocrystal. This indicates that the PL of our sample is due to direct recombination inside the confined exciton, an interpretation that is confirmed by the redshift of the PL maximum wavelength as the nanocrystal size and effective gap grow by annealing at increasing temperatures. The Stokes shift of the PL is hence rather small in our samples, in accordance with observations of colloidal PbS nanocrystals.²⁷ This is in strong contrast to the case of cadmium chalcogenide nanocrystals grown in similar glass hosts: in that case, the PL is due to transitions between states in excitons that are trapped on nanocrystal surfaces, and such states display a large Stokes shift.²⁸ More detailed emission property studies²⁹ show that PbS nanocrystals synthesized in the way described here have a higher excitation cross section than that of Er in glasses and display a temperature-dependent radiative lifetime ascribed to the presence of a dark exciton state. Such results enhance the value of this hybrid synthesis scheme for the use of PbS-doped glasses in optical applications. In the following, we reverse this approach and use PL to monitor growth properties, assuming that the PL maximum is always close to the effective gap of our nanocrystals.

C. Controlling nanocrystal nucleation and growth

Nanocluster nucleation and initial growth can only occur via component species' mobility. Systematic studies³⁰ have shown that for the majority of metal ions in glasses, significant mobility only sets in at temperatures within 10%–15% of T_g . Hence there is a kinetic limitation to the process, possibly involving collective motion in the glass. For PbS nanocluster synthesis in our S-implanted lead-containing glasses, annealing at 440 °C, well below T_g , leads to a PL intensity increase at a fixed wavelength of about 1 μm [Fig. 3(a)]. We interpret this result as an increase in the number of PbS nanocrystals ("nucleation regime") with a mean radius $\langle R \rangle \approx 1.9$ nm. This agrees with the observations on cadmium chalcogenide nanocrystals synthesized by implantation in pure silica^{31,32} in which the earliest stage consists in an increase of the precipitate volume fraction at a constant size of a few nanometers. Unfortunately, in our case the nanocluster size is at the very limit of high-resolution TEM (HRTEM) measuring possibilities for nanoclusters in a glass matrix so that no significant information on the nucleation time evolution may be obtained. On the other hand, when annealed above T_g , the PL shifts to longer wavelengths with little variation in intensity: this behavior [Fig. 3(b)] is ascribed to nanocrystal growth ("growth regime"). Assuming that PL broadening is mostly due to size inhomogeneity and using the size-gap relation, an estimate of the size distribution full width at half maximum (FWHM) is $\text{FWHM}/\langle R \rangle \approx 20\%$ in the nucleation regime and 30%–35% in the growth regime. This is half that observed in (Pb+S) coimplanted silica ($\text{FWHM}/\langle R \rangle \approx 60\%$, confirmed by TEM),¹⁸ demonstrating that our synthesis technique provides rather good control over nucleation and growth of PbS nanocrystals.

Ideally, a direct determination of the nanocrystal radius (via high-resolution transmission electron microscopy, for example) as a function of annealing temperature and time should allow comparison to nucleation and growth models.

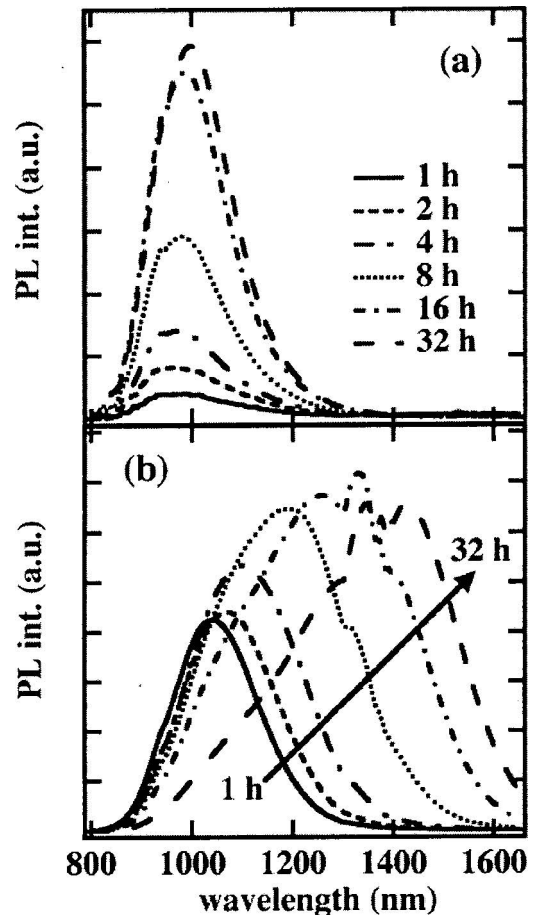


FIG. 3. PL spectra of S-implanted Pb3 glass at (a) 440 °C and (b) 500 °C, after increasing annealing durations. The PL intensity after a 500 °C anneal is one to two orders of magnitude higher than after a 440 °C anneal.

In our case, this approach is unfortunately invalidated by the fact that we deal with a very inhomogeneous PbS nanocrystal density distribution due to the S implantation profile so that usual nucleation and growth schemes assuming homogeneous distributions³³ no longer apply. For example, analytical calculations and simulations³⁴ indicate—and experiments^{13,17} confirm—that the size distribution shape then deviates significantly from the classical Lifshitz–Slyozov–Wagner³⁵ (LSW) coarsening size distribution.

As PbO is easily included into silicate glasses, the use of ion implantation to control the amount of sulfur in the host allows exploration of a broad glass composition range. ZnO is commonly used in glasses designed for lead chalcogenide nanocrystal growth^{5–11} because it improves chalcogenide retention,^{36,37} but it can also affect nucleation and growth, as shown in the case of CdSSe nanocrystals in Zn-containing glasses,^{38,39} where Zn replaced the metal in the chalcogenide composition. Another example is that of extended x-ray-absorption fine structure (EXAFS) studies⁴⁰ showing that while Se is preferentially linked to Zn in ZnO-containing silicate glasses, it is strongly coordinated to oxygen in Zn-free glasses. In order to verify the influence of the ZnO content on nucleation and growth, we progressively replaced CaO by ZnO in an initially Zn-free soda-lime silicate glass

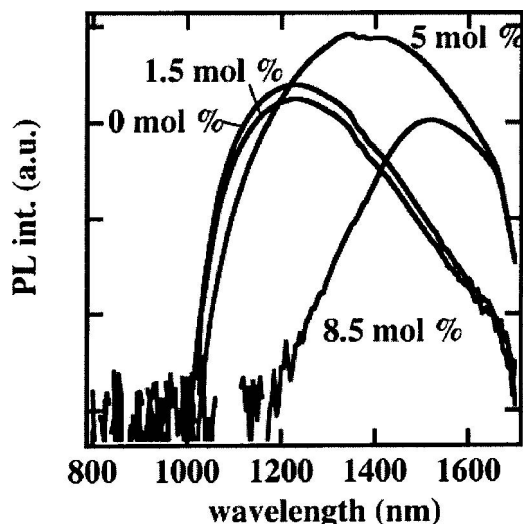


FIG. 4. PL spectra of PbZn glasses (each curve corresponds to a different ZnO molar content) after S implantation and a 2 h postanneal at 600 °C. Note that the ordinate scale is logarithmic.

(see PbZn glasses in Table I) and studied the PL dependence after the same sulfur implantation and heat treatment (2 h at 600 °C) as in the previous case. Figure 4 and Table II show that the redshift of the PL (related to the PbS nanocrystal size) increases with the ZnO concentration. The narrowest PL linewidth (FWHM=180 nm) corresponded to a size distribution of only $\text{FWHM}/\langle R \rangle \approx 15\%$, a figure rarely encountered. This value was obtained for a glass in which CaO was entirely replaced by ZnO; its PL was centered at 1.53 μm , demonstrating the possibilities of our technique for designing an highly doped optically active medium in the optical telecommunication wavelength range. The PL line intensity was some ten times higher for a ZnO concentration of 5 mol %; its FWHM was then about 250 nm, corresponding to a size distribution of ca. 25%. We note that the PL intensity varied by about an order of magnitude depending on whether low- or high-ZnO-concentration (or mixed ZnO–CaO) glasses were used, whereas the glasses were all implanted with the same S fluence. This is another clear manifestation of the complex chemistry leading to growth of PbS nanocrystals in oxide glasses.¹⁸

What is the effect of an increased Zn content on nucleation and growth of PbS nanocrystals? Nanocrystal growth is faster because Zn weakens S bonding to the glass network⁴⁰ and thus S is more likely to diffuse. On the other hand, the nucleation rate of PbS (and hence the PL intensity) is somewhat lower in Zn-rich glasses because Pb competes with Zn in binding to chalcogenides. With zinc diffusion being faster than that of Pb in silicates,⁴¹ we conjecture that (an unknown

TABLE II. PL spectra wavelength (λ), full width at half maximum (FWHM), and intensity (I) for S-implanted PbZn glasses postannealed for 2 h at 600 °C (see Fig. 4).

	PbZn0	PbZn1	PbZn5	PbZn9
λ (nm)	1240	1240	1380	1530
FWHM (nm)	200	200	250	180
I (a.u.)	0.17	0.25	0.8	0.11

proportion of) ZnS clusters may form initially; whereas later the more stable PbS phase is formed because the PbS bond enthalpy (347 kJ/mol) is higher than that of ZnS (205 kJ/mol).⁴² This would explain why the maximum PL intensity is reached when the mixed ZnO–CaO glass is used as host. In a Zn-free glass, PbS precipitation could be hindered by the slow lead diffusion within the glass, leading to a very small growth rate. At high Zn concentrations, sulfur may diffuse faster, accelerating PbS growth, but ZnS nanocluster formation could limit the volume fraction of PbS nanoclusters. The optimum yield for PbS nanoclusters would then be reached for a mixed CaO–ZnO glass due to a trade-off between the Zn-aided S diffusion which accelerates PbS nanocluster growth and the drawback of ZnS nanocluster formation. The maximum precipitation efficiency is obtained at the expense of growth control, the size distribution broadening (hence the PL spectrum width) being enhanced, probably by competing Zn-free versus Zn-rich nucleation and growth mechanisms.

Finally, we note that if ZnS nanocrystals do grow, their gap is at least 3.6 eV, hence their PL is centered at wavelengths well above those observed here and does not contribute to our spectra. On the other hand, an effect of Zn impurity (or nanocluster) absorption on the PL excitation mechanism of PbS nanocrystals cannot be excluded at this stage.

IV. CONCLUSION

We have successfully synthesized PbS nanocrystals by annealing (around T_g) a sulfur-implanted Pb-containing silicate glass. In doing so, we circumvented two major drawbacks of previous methods. The use of S implantation helps us to overcome the retention problem of traditional methods, and the concomitant possibility of accessing a wide range of Pb-containing glass compositions allows rather precise PbS nanocrystal nucleation and growth control. The technique is therefore far more effective than sequential implantation of the components in pure silica. Combined with this hybrid technique, the addition of Zn to the Pb-glass composition should allow fabrication of waveguides doped with a high volume fraction of PbS nanocrystals, whose relatively narrow size distribution (ca. 15% at a wavelength of 1.53 μm) is of considerable interest for optical telecommunications.

ACKNOWLEDGMENTS

We are grateful to O. Kaitasov and S. Collin for considerable technical assistance and to F. Priolo for insightful comments.

¹H. J. Eisler, V. C. Sundar, M. G. Bawendi, M. Walsh, H. Smith, and V. Klimov, *Appl. Phys. Lett.* **80**, 4614 (2002).

²M. A. Petruska, A. V. Malko, P. M. Voyles, and V. Klimov, *Adv. Mater. (Weinheim, Ger.)* **15**, 610 (2003).

³K. Wundke, S. Pötting, J. Auxier, A. Schülzgen, N. Peyghambarian, and N. F. Borrelli, *Appl. Phys. Lett.* **76**, 10 (2000).

⁴G. Tamulaitis, V. Gulbinas, G. Kodis, A. Dementjev, L. Valkunas, I. Motchalov, and H. Raaben, *J. Appl. Phys.* **88**, 178 (2000).

⁵N. F. Borrelli and D. W. Smith, *J. Non-Cryst. Solids* **180**, 25 (1994).

⁶G. Kellermann, A. F. Craievitch, L. C. Barbosa, and O. L. Alves, *J. Non-Cryst. Solids* **293–295**, 517 (2001).

- ⁷B. G. Potter and J. H. Simmons, *Phys. Rev. B* **37**, 10838 (1988).
- ⁸G. P. Banfi, V. Degiorgio, and B. Speit, *J. Appl. Phys.* **74**, 6925 (1993).
- ⁹V. Esch *et al.*, *Phys. Rev. B* **42**, 7450 (1990).
- ¹⁰E. V. Kolobkova, A. A. Lipovskii, N. V. Nikonorov, and A. A. Sitnikova, *Phys. Status Solidi A* **147**, K65 (1995).
- ¹¹A. A. Lipovskii, E. V. Kolobkova, and V. D. Petrik, *J. Cryst. Growth* **184/185**, 365 (1998).
- ¹²A. Meldrum *et al.*, *Mater. Res. Soc. Symp. Proc.* **536**, 317 (1999).
- ¹³A. Meldrum, E. Sonder, R. A. Zuhr, I. M. Anderson, J. D. Budai, C. W. White, L. A. Boatner, and D. O. Henderson, *J. Mater. Res.* **14**(12), 4489 (1999).
- ¹⁴C. W. White *et al.*, *Mater. Res. Soc. Symp. Proc.* **504**, 399 (1999).
- ¹⁵A. Meldrum, C. W. White, L. A. Boatner, I. M. Anderson, R. A. Zuhr, E. Sonder, J. D. Budai, and D. O. Henderson, *Nucl. Instrum. Methods Phys. Res. B* **148**, 957 (1999).
- ¹⁶R. Espiau de Lamaestre, H. Bernas, and F. Jomard, *Nucl. Instrum. Methods Phys. Res. B* **216**, 402 (2004).
- ¹⁷R. Espiau de Lamaestre and H. Bernas (unpublished).
- ¹⁸R. Espiau de Lamaestre, J. Majimel, F. Jomard, and H. Bernas, *J. Phys. Chem. B* **109**, 19148 (2005).
- ¹⁹M. B. Volf, *Chemical Approach to Glass* (Elsevier Science, New York, 1984), p. 524.
- ²⁰J. E. Shelby, *Handbook of Gas Diffusion in Solids and Melts* (ASM International, Materials Park, OH, 1996), p. 191.
- ²¹J. Chaumont, F. Lalu, and M. Salomé, *Nucl. Instrum. Methods* **189**, 193 (1981).
- ²²J. F. Ziegler, J. P. Biersack, and U. Littmark, *The Stopping and Range of Ions in Solids* (Pergamon, New York, 1985).
- ²³Y. Wang and N. Herron, *Phys. Rev. B* **42**, 7253 (1990).
- ²⁴R. Espiau de Lamaestre, H. Bernas, Ch. Ricolleau, and J. Majimel, *Nucl. Instrum. Methods Phys. Res. B* (in press).
- ²⁵H. D. Schreiber, S. J. Kozak, G. B. Balzas, A. L. Fritchman, and C. W. Schreiber, *J. Am. Chem. Soc.* **72**, 1680 (1989).
- ²⁶R. Espiau de Lamaestre, F. Jomard, J. Majimel, and H. Bernas, *J. Non-Cryst. Solids* **351**, 3031 (2005).
- ²⁷M. J. Fernée, A. Watt, J. Warner, S. Cooper, N. Heckenberg, and H. Rubinsztein-Dunlop, *Nanotechnology* **14**, 991 (2003).
- ²⁸V. Jungnickel and F. Henneberger, *J. Lumin.* **70**, 238 (1996).
- ²⁹R. Espiau de Lamaestre, H. Bernas, D. Pacifici, G. Franzo, and F. Priolo (unpublished).
- ³⁰C. Rüssel, *J. Non-Cryst. Solids* **134**, 169 (1991).
- ³¹A. Ekimov, *J. Lumin.* **70**, 1 (1996).
- ³²O. Lublinskaya, S. Gurevich, A. Ekimov, I. Kudryavtsev, A. Osinskii, M. Gandais, and Y. Wang, *J. Cryst. Growth* **184/185**, 360 (1998).
- ³³L. Ratke and P. W. Voorhees, *Growth and Coarsening* (Springer, Berlin, 2002).
- ³⁴V. A. Borodin, K. H. Heinig, and S. Reiss, *Phys. Rev. B* **56**, 5332 (1997).
- ³⁵I. M. Lifshitz and V. V. Slyozov, *J. Phys. Chem. Solids* **19**, 35 (1961); C. Wagner, *Z. Elektrochem.* **65**, 581 (1961).
- ³⁶R. R. Shively, Jr. and W. A. Weyl, *J. Am. Ceram. Soc.* **30**, 311 (1947).
- ³⁷A. Dietzel, *Glastech. Ber.* **1**, 1 (1941).
- ³⁸S. Brekhovskikh, G. Galimov, Y. Nikomov, P. A. Neich, and L. Semina, *Sov. J. Glass Phys. Chem.* **6**, 231 (1980).
- ³⁹N. F. Borelli, D. W. Hall, H. J. Holland, and D. W. Smith, *J. Appl. Phys.* **61**, 5399 (1987).
- ⁴⁰A. Ramos, C. Levelut, and J. Petiau, *J. Non-Cryst. Solids* **151**, 13 (1992).
- ⁴¹W. Chengyu and Z. Xuelu, *Glastech. Ber.* **60**, 324 (1987).
- ⁴²*CRC Handbook of Chemistry and Physics* edited by D. R. Lide (CRC, Boca Raton, 2000).

Evidence for a “dark exciton” state of PbS nanocrystals in a silicate glass

R. Espiau de Lamaëstre

CSNSM-CNRS, Université Paris XI, 91405-Orsay, France and Fontainebleau Research Center, Corning SAS, 77210 Avon, France

H. Bernas^{a)}

CSNSM-CNRS, Université Paris XI, 91405-Orsay, France

D. Pacifici, G. Franzó, and F. Priolo

MATIS-INFN and Dipartimento di Fisica e Astronomia, Via Santa Sofia 64, I-95123 Catania, Italy

(Received 24 December 2005; accepted 21 March 2006; published online 4 May 2006)

PbS nanocrystals (diameter of 5–7 nm) were synthesized via sulfur ion implantation in Pb-based glasses and postannealing. They display strong emission at around 1.5 μm due to quantum confinement, and a very large photoluminescence (PL) excitation cross section. The PL intensity and decay rate temperature dependences provide evidence for a large energy splitting (ca. 30 meV) of the emitting exciton ground state fine structure, presumably due to the complex PbS electronic band structure. © 2006 American Institute of Physics. [DOI: 10.1063/1.2201885]

The optical properties of lead chalcogenide nanocrystals^{1–4} are particularly interesting because of (i) their electronic band structure due to an unusual rocksalt crystallographic structure and (ii) the easily obtained “strong confinement” character of both electron and hole for nanocrystals. For PbS nanocrystals, the small band gap and effective mass allow controlled light emission tuning from about 3 μm to the visible range by decreasing their size, making them attractive candidates for optically active materials in the midinfrared (IR) range.

A major obstacle to their study is the difficulty of PbS nanocrystal growth control in glasses except in limited cases.^{5,6} We developed a versatile synthesis method⁷ by implanting sulfur into a broad range of PbO-containing glasses, and found intense photoluminescence (PL) emission ascribed to direct recombination of the confined PbS nanocrystal exciton. Here, we present measurements of the excitation cross section of PbS nanocrystals emitting at around 1.5 μm (size \approx 7 nm), and of temperature-dependent PL intensities and lifetimes. Our results provide evidence for a splitting of the exciton ground state with a long-lived (“dark exciton”) state lying below a short-lived (“bright”) state, as found in CdSe (Refs. 8 and 9) and Si nanocrystals,¹⁰ but with major differences due to the unusual electronic structure^{11,12} of PbS nanoclusters.

Polished samples of a Pb-containing silicate glass (73 SiO₂, 16 CaO, 10 CaO, and 1 PbO mol %) were implanted with 150 keV sulfur ions (fluence of $3.4 \times 10^{15} \text{ cm}^{-2}$). A 1 h postanneal at 675 °C promoted nucleation and growth of PbS nanocrystals, as evidenced by transmission electron microscopy (TEM).⁷ Time-resolved PL experiments were performed with an Ar ion laser (488 nm line) chopped at 55 Hz by an acousto-optic modulator. The laser beam was focused (0.3 mm radius spot) on the sample surface and sample emission was in the linear excitation regime. PL was collected by lenses and dispersed by a spectrograph, and detected via a near-IR Hamamatsu photomultiplier tube. The overall system response time (30 ns) was ten times shorter than the fastest

transient signal observed. Standard PL spectra were detected via a liquid nitrogen cooled Ge detector and acquired with a lock-in amplifier using the acousto-optic modulator frequency as a reference.

Excitation features of excitons confined in semiconductor nanocrystals are often approximated by a two-level system.¹³ Using a linear rate equation with this model, the total lifetime τ is $\tau^{-1} = \tau_r^{-1} + \tau_{nr}^{-1}$, where τ_r and τ_{nr} are the radiative and nonradiative lifetimes, respectively. The PL intensity is proportional to the number of nanocrystals in the excited state N^* optically pumped by a photon flux ϕ and to the radiative recombination rate,

$$I_{\text{PL}} \propto N^* \tau_r^{-1}. \quad (1)$$

Upon excitation, the emitted intensity increase is an exponential with

$$\tau_{\text{on}}^{-1} = \sigma\phi + \tau^{-1}, \quad (2)$$

where σ is the excitation cross section.

Figure 1 shows PL spectra at three different temperatures in the range of 11–290 K of a sample whose emission is centered at 1.4 μm and inhomogeneously broadened [full width at half maximum (FWHM)=350 nm]. The relation between size and effective gap,¹⁴ neglecting the small Stokes shift,² leads to a mean PbS nanocrystal radius of 2.8 nm, consistent with the average radius of 3.5(0.5) nm measured

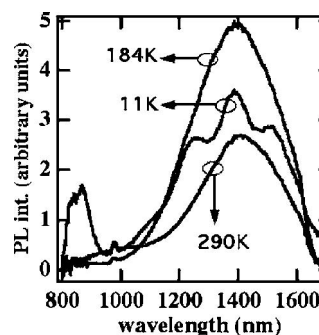


FIG. 1. Photoluminescence spectra taken at three different temperatures for a sample containing PbS nanocrystals. The laser pump power was 45 mW.

^{a)}Author to whom correspondence should be addressed; electronic mail: bernas@csnsm.in2p3.fr

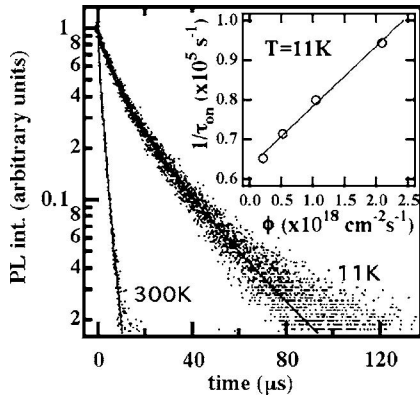


FIG. 2. (a) PL time decay curves at $T=11$ and 300 K taken at the maximum PL emission wavelength ($\lambda=1400$ nm). The lines are stretched exponentials with $\tau=1.7$ μs and $\beta=0.78$ ($T=300$ K), and $\tau=12.5$ μs and $\beta=0.7$ ($T=11$ K). The laser pump power was 45 mW. (b) PL rise rate $1/\tau_{\text{on}}$ vs photon flux ϕ at $\lambda=1.4$ μm measured at 11 K.

by TEM (Ref. 7) on a sample emitting at 1.55 μm . PL decay measurements performed at 11 K and at room temperature are shown in Fig. 2. Decay times are some three orders of magnitude larger than those of direct exciton recombination in II-VI nanocrystals,⁹ due to the enhanced local field factor acting on the spontaneous recombination rate of the first exciton transition in lead salts.² Ignoring excitonic state perturbation by shape and interface effects for simplicity,² we compute $\tau_r=0.3$ μs for a 3.5 nm radius PbS nanocrystal (corresponding to an effective gap ca. 0.8 eV), compared with a measured value of 1.7 μs . The discrepancy is acceptable in view of our approximation, and does not jeopardize our interpretation in terms of confined exciton recombination. Due to exciton hopping between nanocrystals¹⁵ or to sample inhomogeneities,⁹ the PL decay (Fig. 2) is described by stretched exponentials, $I(t)=I_0 \exp[-(t/\tau)^\beta]$, where τ is an effective decay time and β a constant between 0 and 1 . At 300 K we find $\tau=1.7$ μs and $\beta=0.78$, while at 11 K we obtain $\tau=12.5$ μs and $\beta=0.7$.

The very low surface concentration of nanocrystals precluded a direct determination of the excitation cross section from an optical transmission measurement. However, PL rise times at $T=11$ K and $\lambda=1400$ nm were measured as a function of photon flux. The results followed Eq. (2) (see inset of Fig. 2): the intercept corresponds to a lifetime $\tau_r=15.8$ μs , within 20% of the value obtained in the direct measurement of Fig. 2. From its slope, we deduce an excitation cross section $\sigma=1.5 \times 10^{-14}$ cm^2 . The latter (at 488 nm) is 10^5 times higher than typical values for Er emission in optical fibers at 1.54 μm and two orders of magnitude higher than those reported for Si nanocrystal-sensitized Er emission.¹⁶ This result clearly provides strong incentive for a direct optical gain measurement.

We emphasize that nonradiative recombinations do not provide a major contribution to the decay time temperature dependence of Fig. 2, since the PL intensity increases between 11 and 180 K (Fig. 1), whereas the decay time decreases continuously as the temperature rises. The radiative rate is therefore temperature dependent. Figure 3 displays the PL intensity (a) and decay time (b) as a function of temperature for two different emission wavelengths (1.4 μm , triangles; 1.6 μm , squares). Assuming that the average absorption cross section remains constant between 11 and 300 K and hence that the excitation rate $\sigma\phi \cong 10^{-2}$ μs^{-1} is negli-

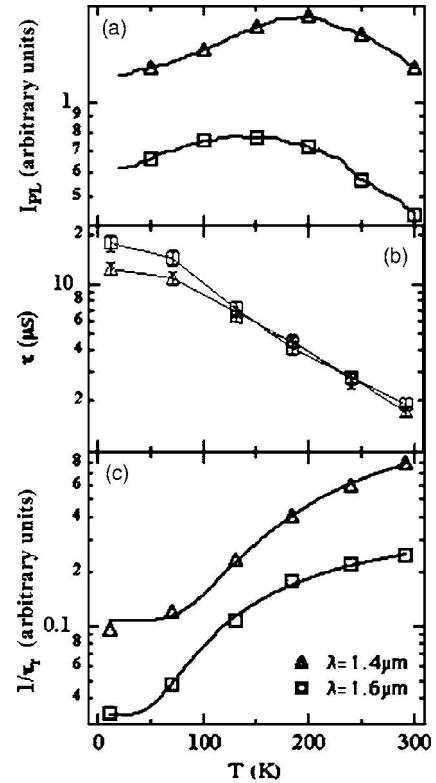


FIG. 3. Temperature dependence at low power density (0.3 W cm^{-2}), and two different emission wavelengths of (a) PL intensity and (b) PL decay time, and (c) radiative lifetime of PbS nanocrystals. Full lines in (c) are fits to Eq. (3).

gible as compared with the experimental recombination rates τ^{-1} , we deduce a radiative recombination rate temperature dependence [Fig. 3(c)] similar to those^{10,16,17} due to the quantum confinement-enhanced electron-hole exchange interaction. The energy splitting Δ between exciton states is usually^{18,19} in the 1 – 10 meV range, and PL emission from the triplet (dark exciton) state to the singlet ground state is partially allowed due to spin-orbit interaction mixing. If $k_B T < \Delta$ the triplet state alone is populated and the radiative emission lifetime increases, whereas if $k_B T \gg \Delta$ both states are populated, the radiative lifetime is reduced, and the quantum yield increased. The effective radiative lifetime τ_r of the system can be expressed¹⁷ in terms of both singlet τ_S and triplet τ_T state radiative lifetimes:

$$\frac{1}{\tau_r} = \frac{3/\tau_T + (1/\tau_S)\exp(-\Delta/k_B T)}{3 + \exp(-\Delta/k_B T)}. \quad (3)$$

Fitting our results to Eq. (3) [Fig. 3(c)] we find at 1.4 μm (1.6 μm) $\tau_T/\tau_S=18 \pm 2$ (5.2 ± 0.4) and $\Delta=37 \pm 3$ meV (22 ± 2 meV). The splitting Δ is much larger than in CdSe and Si nanocrystals and in strong disagreement with the only available estimate of the PbS exchange interaction.¹¹ This is presumably due to the latter's failure in describing the lowest excitation level's fine structure. Other factors that influence the fine structure and hence Δ for PbS are the band anisotropy¹² mixing of states with different parities, the electron-hole Coulomb interaction, and the existence of intervalley scattering¹¹ resulting from direct band gap at four equivalent Brillouin zone L points. All await detailed evaluation.

In conclusion we offer evidence for the existence of a "dark exciton" state in IV-VI nanocrystals, although a more

complete description of the first exciton level's fine structure is clearly required. The efficient emission from PbS nanocrystals around $1.5 \mu\text{m}$ and the correspondingly large excitation cross sections suggest that this system may be a promising alternative for future optical amplifiers or low power fast saturable absorbers.

The authors are grateful to C. Delerue and B. Sermage for insightful remarks, and to O. Kaitasov and S. Collin for technical assistance.

- ¹S. W. Buckner, R. L. Konold, and P. A. Jelliss, *Chem. Phys. Lett.* **394**, 400 (2004).
- ²B. L. Wehrenberg, Congjun-Wang, and P. Guyot-Sionnest, *J. Phys. Chem. B* **106**, 10634 (2002).
- ³L. Bakueva, G. Konstantatos, L. Levina, S. Musikhin, and E. H. Sargent, *Appl. Phys. Lett.* **84**, 3459 (2004).
- ⁴A. Olkhovets, R.-C. Hsu, A. Lipovskii, and F. W. Wise, *Phys. Rev. Lett.* **81**, 3539 (1998).
- ⁵N. F. Borelli and D. W. Smith, *J. Non-Cryst. Solids* **180**, 25 (1994).
- ⁶A. A. Lipovskii, E. V. Kolobkova, A. Olkhovets, V. D. Petrikov, and F.

- Wise, *Physica E (Amsterdam)* **5**, 157 (1999).
- ⁷R. Espiau de Lamaestre and H. Bernas, *J. Appl. Phys.* **98**, 104310 (2005).
- ⁸M. Nirmal, D. J. Norris, M. Kuno, and M. G. Bawendi, *Phys. Rev. Lett.* **75**, 3728 (1995).
- ⁹O. Labeau, P. Tamarat, and B. Lounis, *Phys. Rev. Lett.* **90**, 257404 (2003), and references therein.
- ¹⁰M. L. Brongersma, P. G. Kik, A. Polman, K. S. Min, and H. A. Atwater, *Appl. Phys. Lett.* **76**, 351 (2000), and references therein.
- ¹¹I. Kang and F. W. Wise, *J. Opt. Soc. Am. B* **14**, 1632 (1997).
- ¹²G. E. Tudury, M. V. Marquezini, L. G. Ferreira, L. C. Barbosa, and C. L. Cesar, *Phys. Rev. B* **62**, 7357 (2000).
- ¹³S. Schmitt-Rink, D. A. B. Miller, and D. S. Chemla, *Phys. Rev. B* **35**, 8113 (1987).
- ¹⁴Y. Wang and N. Herron, *Phys. Rev. B* **42**, 7253 (1990).
- ¹⁵J. Heitmann, F. Müller, Lixin Yi, M. Zacharias, D. Kovalev, and F. Eichhorn, *Phys. Rev. B* **69**, 195309 (2004).
- ¹⁶D. Pacifici, G. Franzò, F. Priolo, F. Iacona, and L. Dal Negro, *Phys. Rev. B* **67**, 245301 (2003).
- ¹⁷P. D. J. Calcott, K. J. Nash, L. T. Canham, M. J. Kane, and D. Brumhead, *J. Lumin.* **57**, 257 (1993).
- ¹⁸T. Takagahara and K. Takeda, *Phys. Rev. B* **53**, 4205 (1996).
- ¹⁹E. Martin, C. Delerue, G. Allan, and M. Lannoo, *Phys. Rev. B* **50**, 18258 (1994).

Significance of lognormal nanocrystal size distributions

R. Espiau de Lamaëstre^{1,2} and H. Bernas^{1,*}

¹*CSNSM/CNRS, Université Paris Sud, 91405 Orsay Campus, France*

²*Fontainebleau Research Center, Corning SAS, 77210 Avon, France*

(Received 14 June 2005; revised manuscript received 14 November 2005; published 15 March 2006)

Metallic or semiconductor nanocrystals produced by very different techniques often display size distributions whose limiting shape (e.g., after long annealing times) is self-preserving and close to lognormal. We briefly survey the diverse microscopic mechanisms leading to this behavior, and present an experimental study of its inception in the case of semiconducting nanocrystals synthesized by ion implantation in silica. This example shows how the ultimate lognormal distribution is related to the system's memory loss of initial nucleation and growth processes.

DOI: [10.1103/PhysRevB.73.125317](https://doi.org/10.1103/PhysRevB.73.125317)

PACS number(s): 64.75.+g, 81.07.-b, 05.40.-a, 85.40.Ry

I. INTRODUCTION

Many nanoscience studies involve attempts¹ to control nanocrystal average sizes and size distributions. Narrowing the latter is rarely easy. In specific cases, excellent results may be obtained by special chemical (notably colloidal² and sol-gel³) reactions. More often, reasonably narrow size distributions are the outcome of a carefully controlled nucleation and growth process. This implies an appropriate understanding of the process; typically, this is obtainable in a quasiequilibrium thermodynamics situation such as that of Ostwald ripening, where an analytical formulation of the long-term limit of the size distribution was obtained.^{4,5} This is the so-called Lifshitz-Slyosov-Wagner (LSW) treatment,

$$f_{LSW}(R=r) = n_0 \left(\frac{\langle R \rangle_0}{\langle R(t) \rangle} \right)^3 \tilde{f} \left(\frac{r}{\langle R(t) \rangle} \right), \quad (1)$$

$$\tilde{f}(z) = 3^4 2^{-5/3} e z^2 (z+3)^{-7/3} (3/2-z)^{-11/3} \exp \frac{1}{2z/3-1}, \quad (2)$$

where n_0 is some initial nanocrystal density of mean radius $\langle R \rangle_0$, and $\langle R(t) \rangle$ is the mean nanocrystal radius at time t .

In attempting⁶ to broaden this approach experimentally, we encountered several instances in which the final size distribution was apparently lognormal as in Eq. (3), where μ is the geometric average and σ the geometric standard deviation:

$$f_{\text{lognormal}}(R=r) = \frac{1}{r \ln \sigma \sqrt{2\pi}} \exp \left(-\frac{(\ln r/\mu)^2}{2(\ln \sigma)^2} \right). \quad (3)$$

A search through the literature shows that this distribution is quite common⁷ in many fields of physics and biophysics. To our knowledge, with the few exceptions referenced below it has rarely been discussed in the case of nanocluster synthesis in “hard” condensed matter, and there are no systematic experimental studies of its origin in that case. We report the results of our attempt to determine whether—and possibly how—physical information is obtainable on nanocrystal nucleation and growth from such a size distribution shape. Hopefully, this paper will stimulate further work in an area

which may contribute greatly to nanocrystal size control.

The diversity of processes leading to lognormal size distributions is the first thing to emphasize. Aggregation of colloids⁸ or of aerosols,⁹ some crystallization processes,^{10,11} some complex nucleation and growth processes,^{12–15} all may lead to limiting size distributions that display apparently lognormal shapes. The fact that these processes involve very different microscopic mechanisms is clearly indicative of a very general property that we aimed to discern. This involved other questions. Where does the generality of lognormal shapes come from? Or conversely, what information on the physical process(es) occurring in an evolutionary system is contained in the lognormal distribution? For nanocrystals, if a nucleation and growth process leads to this limiting form of the size distribution, can the lognormal shape provide information on the differences between this process and that which leads to the LSW shape?

We encountered this problem in attempting to control the nucleation and growth of nanocrystals after ion implantation and/or irradiation. The main advantage of such techniques is to allow supersaturation of a solute in the host, but they also produce instabilities that lead away from equilibrium thermodynamics (radiation-enhanced or -induced diffusion, metastable compound formation, etc.). When pure metal clustering was involved, we found a case¹⁶ in which nanocrystal synthesis led to a limiting size distribution corresponding almost exactly to the LSW prediction. On the other hand, many other ion-induced syntheses^{12–15} gave rise to lognormal distributions. This paper reports a study of the latter observation's origin. For reference, Sec. II provides a brief survey of the phenomena leading to lognormal size distributions and precipitation in inhomogeneous systems. Section III reports a specific experimental study of a system produced by sequential implantation of two different elements in silica followed by postannealing. We show how a rather complex sequence (chemical solute-host interactions, ionic diffusion, nucleation and growth) lead to a well-defined lognormal size distribution as the limiting shape. In Sec. IV, based on the general approach of Binder,¹⁷ we discuss the dynamics leading from the microscopic physical processes listed above to their translation in terms of a given size distribution. We show, in the case of nanocrystals grown after ion beam synthesis, that the multiplication of nucleation and

growth paths blurs the information contained in the size distribution. We relate this loss of information to the lognormal shape of the size distribution. In the perspective of the present work, ion beam synthesis has the advantage of multiplying—in a rather well-controlled way—interfering nucleation and growth mechanisms, but it should be noted that such effects are also encountered in many other growth situations, including coagulation.

Besides their interest as quantum systems, metallic or low-band-gap compound semiconductor nanocrystals in waveguide materials are of interest for photonics devices. The key parameters to be controlled are, besides the mean radius of the nanocrystals, precisely their size distribution and density. The results obtained here may therefore be of interest for both basic and applied physics.

II. GENERAL REMARKS

A. When are size distributions lognormal? A brief survey

Lognormal distributions are encountered in many areas of growth science. In the fields of cluster aggregation and coagulation, for example, considerable work has been done to link experimentally observed lognormal cluster size distributions to theoretical descriptions based on the initial work of Von Smoluchowski¹⁸ regarding the coagulation process. He developed equations based on the following assumptions: (i) cluster formation starts from a population of monomers, and proceeds by successive binary collisions between clusters of any size; (ii) these binary collisions between species lead to *irreversible* coalescence, i.e., once formed, clusters can never become smaller. Thus, if n_k be the concentration of k -mers and K_{ij} the reaction rate constant between i - and j -mers, the time dependence of the k -mer concentration is given by

$$\frac{dn_l}{dt} = \frac{1}{2} \sum_{l'=1}^{l-1} K_{l',l-l'} n_{l'} n_{l-l'} - n_l \sum_{l'=1}^{\infty} K_{l',l} n_{l'}. \quad (4)$$

In the literature, the K_{ij} are referred to as the kernels of the coagulation process. They describe the specific microscopic mechanism by which coagulation proceeds. For clusters diffusing in a solvent or a solid medium, depending on the medium density, coalescence occurs after collisions with both surrounding medium molecules and other clusters (Brownian regime), or with other clusters (ballistic regime). Thus, a cluster mean free path may be defined, involving a collision with another cluster, a monomer, or a solvent molecule. The amplitude of the mean free path depends on the nature of the medium, the solute volume fraction, etc.; it may also vary with the cluster size. As regards Brownian coagulation, theoretical developments by Friedlander *et al.*¹⁹ showed that the asymptotic size distribution is self-preserving and close to a lognormal shape. In this regime, the mean free path of the cluster is smaller than their size, and growth can occur via cluster-cluster aggregation. These conclusions were supported by experimental evidence²⁰ as well as by numerical solutions of discrete kinetic equations.²¹ Self-preserving distributions close to lognormal shapes were also observed for aggregation regimes with microscopic mechanisms differing from Brownian aggregation:

e.g., steady-state shear²² and ballistic or free molecular regimes²³ where the cluster mean free path was larger than its size. Asymptotic size distributions close to lognormal are also expected²⁴ in cases where the aggregates have fractal shapes. All these results were obtained for *closed* systems where an initially large population of particles or clusters coagulate, and they are independent of the initial state of the system.

Lognormal size distributions are also encountered after growth in *open* systems, such as in ultrafine particles synthesis by metal evaporation.^{10,11} In the latter case, a growth-time model was developed to explain the lognormal shape of the size distribution:²⁵ evaporated metal particles form a layer above the bulk; a combination of particle diffusion and drift through this finite growth region leads to a lognormal growth-time probability density. Since the particle radius follows a power law of its growth duration, a lognormal distribution of growth times leads to a lognormal distribution of nanocrystal radii.

Lognormal size distributions have also been reported after nanocrystal formation after postannealing growth in Au-implanted silica,¹² GaN nanocrystals synthesis (by sequential Ga and N implantation and annealing) in dielectrics,¹³ or postimplantation metal nanocrystal formation in Al.^{14,15} In these examples, growth often occurs beyond the initial solute implantation range, and is usually limited by the diffusion of the implanted species. No link between the microscopic mechanisms and the observed size distribution shape was proposed and this paper aims at filling this gap. In Sec. III, we shall relate these results to the degree of information on the microscopic processes as growth proceeds: we show that they actually signal a loss of control over the growth process.

B. Precipitation in inhomogeneous systems

As discussed by Binder,¹⁷ the asymptotic shape of a cluster size distribution is expected to depend on the nature of the physical system as well as on its growth mechanism. In the case of nanocrystal growth, it is interesting to contrast experimentally observed shapes with the shape expected from the LSW coarsening mechanism,^{4,5} via condensation in a binary alloy solid phase, assuming a *uniform* average solute distribution. This leads to a well-defined asymmetric size distribution that has a tail on the small-precipitate side. The origin of size distribution broadening in the latter, as the cluster volume fraction increases, is the varying diffusional interaction between the solute concentration fields around the clusters.

When dealing with inhomogeneous systems, it is worthwhile introducing the screening length λ , which describes the concentration field interaction of neighboring clusters:

$$\lambda = \frac{1}{\sqrt{4\pi\langle R \rangle n}} \quad (5)$$

where n is the average cluster density and $\langle R \rangle$ their average radius. As growth occurs, the increase in average radius does not compensate the reduction in cluster density, so that the screening length progressively increases. The case where the solute distribution is *nonuniform*, as would be the case for an

ion-implanted sample with an implanted profile width Δ , was studied by Trinkaus²⁶ and Borodin.^{27,28} If $\lambda \ll \Delta$, the local solute concentration nonuniformity may be neglected, and LSW-type growth occurs inside a (narrowed) implant profile. If $\lambda \gg \Delta$, on the other hand, solute diffusion occurs due to the concentration inhomogeneity, and clusters tend to dissolve by outdiffusion from the implant profile. Because of the increase in λ outdiffusion from the implanted layer should always be the main trend, at least as long as rather weak solute concentrations and quasiequilibrium thermodynamics are assumed, and interactions with radiation-induced defects are neglected. As a result, when the solute concentration is non-uniform the LSW equations must be modified to include loss of matter by diffusion (a quantity that now depends on the position in the sample). In other words, there is now a coupling between the system's evolution in real space (i.e., the cluster depth distribution) and in size space (the size distribution).

In the case of nanocrystal precipitation in glasses, the growth process may be complicated by complex solute-host chemical interactions that affect solute diffusion and precipitation thermodynamics. We have discussed these effects in some detail for lead chalcogenide nanocrystal growth in pure silica.^{6,29} Here, we show how they systematically lead to a well-defined size distribution resembling a lognormal one.

III. EXPERIMENT

Our purpose was to set up a series of experiments in which we could deliberately relax one or another controlling factor in our samples, in order to determine whether this would ultimately bring the limiting shape of the size distribution to lognormal. All the samples in these experiments were synthesized by sequential ion implantation of Pb and chalcogens in pure silica at energies such that their initial concentration profiles overlapped. The conditions for sequential ion implantation and annealing were those of our previous work,^{6,29,30} and are summarized in Table I. The anneals were performed in a quartz tube furnace under dry N_2 atmosphere, at temperatures ranging from 800 to 900 °C. Nanocluster identification, radius and density measurements were performed via transmission electron microscopy (TEM) on cross-sectional samples cut from the ion-implanted and annealed glasses, using methods detailed in Ref. 30. The TEM image treatment is summarized in the Appendix. In the following, we first studied the effect of allowing varying amplitudes of Pb and S diffusion by changing the annealing temperature or annealing time (at constant temperature). We then studied—by comparing results from samples implanted with different chalcogens—the effect of changing the chemical interactions of the implanted components in silica. Our previous work^{6,30} revealed a rather strong relation between the implanted components' diffusion and their chemical interactions with the host or among themselves, so that the hierarchy of conditions controlling the systems' evolution is ambiguous. In spite of this ambiguity, quite different initial size distributions led to quasi-identical lognormal limiting shapes after sufficient annealing had occurred.

TABLE I. Samples prepared via ion implantation in silica and annealing to study the evolution of chalcogenide nanocrystal size distributions. The last column shows temperatures and annealing times for each sample.

Samples	Implanted species	Energy (keV)	Fluence (atom cm ⁻²)	Annealing
PbS1	Pb	510	1.4×10^{15}	800 °C/8 h
	Pb	260	10^{15}	900 °C/8 h
	S	110	1.7×10^{15}	
	S	50	1.3×10^{15}	
PbS2	Pb	500	1.2×10^{15}	900 °C/1 h
	Pb	350	6×10^{14}	
	S	110	2×10^{15}	
PbS3	S	100	2.2×10^{15}	900 °C/4 h
	Pb	480	1.4×10^{15}	
CdSe	Cd	500	1.3×10^{15}	900 °C/1 h
	Se	270	2×10^{15}	

A. Preliminary remark

Our study involves ion-implanted samples, hence a deliberately nonuniform initial solute distribution. Based on the previous section's discussion, we first note that the ion implant fluence plays a major role. For a given implantation energy, high implant fluences F lead to high solute concentrations (typically a few percent in the cases referred to above) and hence to a large chemical potential gradient between the implanted and unimplanted layers. The average solute concentration in a profile of width Δ being

$$\langle c \rangle \approx \frac{F}{\Delta}, \quad (6)$$

growth leads to a family of clusters with average radius $\langle R \rangle$ and average density $\langle n \rangle$ given by

$$\langle n \rangle \approx \frac{3\langle c \rangle}{4\pi\langle R \rangle^3 N_a} \quad (7)$$

where N_a is the atomic density of the cluster phase in the host. Combining Eqs. (5)–(7), the average screening length can be written in terms of the fluence according to

$$\lambda \approx \langle R \rangle \sqrt{\frac{\Delta N_a}{3F}}. \quad (8)$$

With the typical implant profile widths (ca. 100 nm) and fluences (ca. 10^{16} atoms cm⁻² or more) of the aforementioned experiments, this leads to very small values of λ compared to Δ , and hence to ripening on a very local scale, and to very large heterogeneities in the cluster growth features inside the implant profile—hence to broad (sometimes even bimodal) size distributions. In order to reduce or avoid such effects, we have chosen to perform implants with fluences at or below 10^{16} atoms cm⁻². Pb and S were sequentially implanted at 480 and 100 keV, forming PbS nanocrystals ($N_a \approx 19$ PbS nm⁻³) by annealing at temperature of the order of 800–900 °C. Samples containing 1.24 at. % PbS were

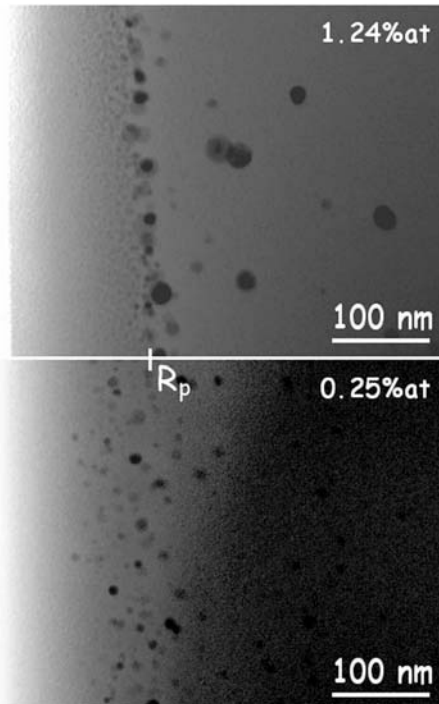


FIG. 1. Illustration of the effect of implant concentration on growth characteristics. Two SiO₂ wafers were sequentially implanted with Pb and S at the same energies, but to different fluences (see text). R_p is the projected range of Pb and S, according to the SRIM code. The 1.24 at. % sample was annealed 1 h at 890 °C and the 0.24 at. % sample was annealed 1 h at 900 °C.

synthesized by implanting fluences of 1.1×10^{16} S cm⁻² and 7×10^{15} Pb cm⁻², and samples containing 0.25 at. % PbS by implanting 2.2×10^{15} S cm⁻² and 1.4×10^{15} Pb cm⁻². In the former samples the screening length is very short (about the nanocrystal size), whereas it is comparable to the profile width in the latter, thus leading us to expect significantly more uniform nanocrystal ripening.

This expectation is borne out by transmission electron microscopy observation of the two nanocrystal families after a 1 h anneal at 900 °C (Fig. 1). In the more concentrated samples, very large clusters around the implant concentration maximum testify to very local ripening; and size inhomogeneities and average size variations as a function of depth are significantly larger, in agreement with observations of other solute-host combinations at comparable concentrations.^{31,32} All further experiments were performed at concentrations below 0.3 at. %. A series of pure silica plates containing chalcogenide nanocrystals was synthesized by ion implantation of group VI and IV elements. The plates were then each cut up to produce identical samples, which were annealed at different temperatures for different times (Table I) and studied via TEM to deduce their depth and size distributions (see Appendix). More information on the experimental procedure and analysis is given elsewhere.^{6,33}

B. When does a size distribution become lognormal?

Figure 2(a) compares the nanocrystal size distributions for

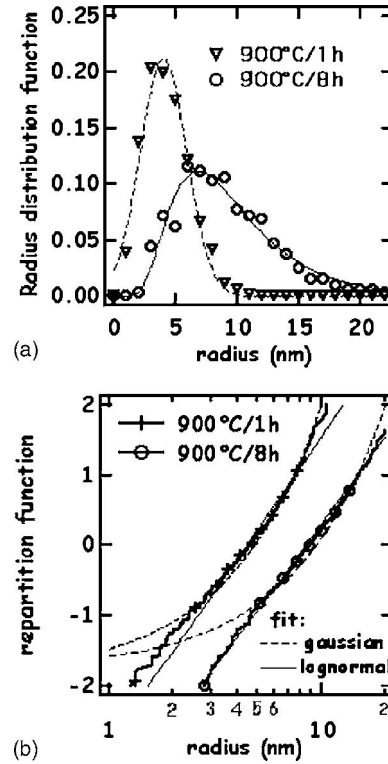


FIG. 2. Experimental radius distribution functions (a) and repartition functions (b) for two samples from PbS1 (Table I) annealed respectively 1 h (inverted triangles) or 8 h (circles) at 900 °C. Full (dashed) lines are lognormal (Gaussian) fits to the data.

identical samples from batch PbS1, annealed at 900 °C for 1 and 8 h, respectively. A 1 h anneal produces a symmetrical Gaussian size distribution around an average radius $R=4.8$ nm, with a standard deviation 1.85 nm (hatched line), whereas the 8 h anneal leads to an asymmetrical distribution, weighted toward larger sizes, that is well fitted to a lognormal (full line). The first two moments (average μ and geometrical standard deviation σ) of the quantity “ln R ” are the fitting parameters of the nanocrystal radii data to the lognormal distribution: we find $\mu=8.65$ nm and $\sigma \approx 1.5$. An accurate way of judging the quality of fit to a lognormal distribution is to enhance the influence of the distribution tails (i.e., higher-order moments) by plotting the repartition function of the radius distribution in Gaussian coordinates.³⁴ The repartition function of a lognormal distribution reads

$$F_{\text{lognormal}}(R < r) = \frac{1}{2} \left[1 + \text{erf} \left(\frac{\ln r / \mu}{\ln \sigma} \right) \right]. \quad (9)$$

Therefore, plotting $\text{erf}^{-1}[2F_{\text{lognormal}}(r)-1]$ as a function of $\ln(r)$ (principal of Gaussian coordinate) gives a straight line whose slope is a simple function of the geometrical standard deviation only. In such a plot, the experimental repartition function is traced by attributing a weight $1/N$ to each measurement of R , where N is the total number of observed nanocrystals. In Fig. 2(b), we have plotted the results of Fig. 2(a) in this way: the 8 h anneal data provide an excellent fit to a straight line with $\sigma=1.47$ (the 1 h anneal data are shown in the same representation for comparison purposes). Several

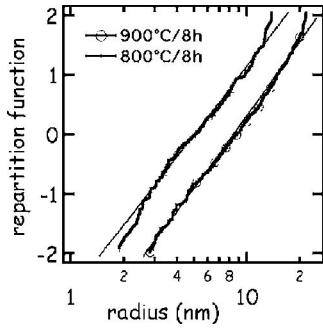


FIG. 3. Influence of annealing temperature on radius repartition function of nanocrystals from PbS1 sample grown at two different temperatures (Table I). Full lines are lognormal fits to the data.

hundred nanocrystals were measured in each run, so that our uncertainty on the geometrical standard deviation is between 2% and 4%. We have thus shown that the size distribution tends to become lognormal when the annealing time increases at a given temperature. As shown in Fig. 3, the same trend occurs when annealing temperature is sufficiently high: the geometrical average of the radius distribution differs, but the shape and geometrical standard deviation are essentially the same.

More generally, obtaining lognormal size distributions was the rule rather than an exception after long-term or high-temperature annealing, including when the implantation profile widths of Pb and S differed or when the implantation sequence was reversed to modify the chemical interaction of the different species with the host.⁶ We also observed nanocrystals size distribution of lognormal shape after sequential implantation synthesis of CdSe nanocrystals (see Table I for implantation parameters and thermal treatment). By normalizing all our radius distributions by their geometrical standard deviation, which is found to be in the range 1.45–1.55 in all cases, we may display the compendium of our results as shown in Fig. 4: the equation of the full line ($\sigma=1.5$) is

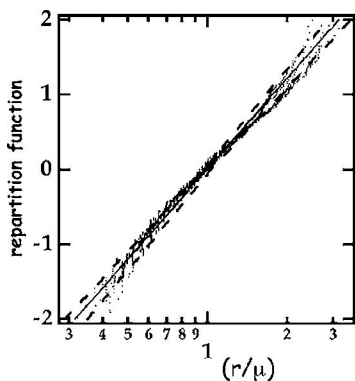


FIG. 4. Radius repartition function (dots) of different samples: PbS1 ($\mu=5.7$ nm) annealed 8 h at 800 °C or ($\mu=8.7$ nm) annealed 8 h at 900 °C; PbS2 ($\mu=3.2$ nm); PbS3 ($\mu=4.7$ nm) annealed 1 h at 900 °C; CdSe ($\mu=5.0$ nm) annealed 1 h at 900 °C. Radii were normalized by the geometrical average radius. Full line, lognormal (geometrical standard deviation 1.5). Dashed lines show the 95% confidence level for the lognormal fit (population 300 precipitates).

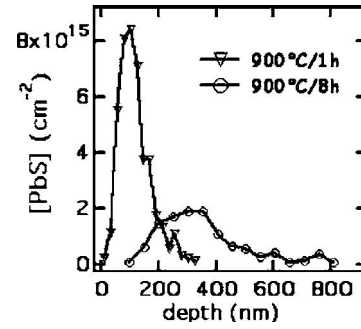


FIG. 5. Comparison (from TEM identification of nanocrystals) of PbS concentration depth dependence for samples from PbS1 after annealing at 900 °C for 1 or 8 h.

$$f_{\text{lognormal}}(z) = \frac{1}{z \ln(1.5) \sqrt{2\pi}} \exp\left(-\frac{[\ln(z)]^2}{2[\ln(1.5)]^2}\right). \quad (10)$$

It is time independent, so that we have an asymptotic distribution; the time dependence is restricted to the geometrical average of the radius distribution, i.e., to the value of μ .

C. How does a size distribution become lognormal?

So far, although our results were obtained by TEM we have plotted the entire size distributions in our figures, regardless of the nanocrystals' depth in the sample. But in inhomogeneous distributions such as these (see Sec. II and Fig. 1), studies of the size distribution cannot be dissociated from a study of the nanocrystal depth dependence. As in our previous work,^{29,31} we found that long-term or high-temperature anneals also produced major changes in the nanocrystal depth distributions. A striking example is given in Fig. 5, which presents the depth distributions for the two samples whose size distributions are shown in Fig. 2, as measured by TEM. Whereas the 1 h anneal at 900 °C leads to cluster nucleation and growth inside the implantation profile limits (≈ 70 –250 nm), and to a Gaussian size distribution, the 8 h annealed sample displays a very broad nanocrystal distribution (up to ≈ 800 nm) and the lognormal size distribution. According to Sec. II annealing leads to an increase in λ in the initially inhomogeneous system, which becomes sensitive to the large chemical potential gradient at the implantation profile edges; nanocrystals then may dissolve in these regions, entailing solute migration. In the case of PbS preferential nucleation and growth of new nanocrystals occurs first at depths corresponding to the implantation profile edges, then at the successive locations of the maximum chemical potential gradient outside of the initial matter concentration profile. Contrary to the process described by LSW, matter is thus not conserved locally, but is transferred progressively outside of the implantation profile.²⁶ Moreover, nucleation and growth occur during the intervening diffusion. These multiple, interfering mechanisms lead to a complex evolution that bears no direct relation to any single process.

Sufficiently long (or high-temperature) annealing thus blurs the system's memory of its initial nanocrystal synthesis process. This may—and does in our case—occur in other

ways, notably due to the fact that the chemical interaction of chalcogens with silica and group VI elements is complex.³⁵ This is shown by a study of nanocrystal size distributions obtained from pure silica sequentially implanted with Pb and a chalcogen, annealed in the same temperature range as previously. Data was taken from the very same TEM samples, in which we separated the size distribution corresponding to nanocrystals inside the central part of the implantation profile from that corresponding to nanocrystals outside of the latter. For samples from Table I that were annealed at sufficiently high temperatures or long times, all distributions were lognormal with $\sigma \approx 1.5$. By contrast, we studied nanocrystal size distributions from pure silica sequentially implanted with Pb and Te, annealed 1 h at 890 °C (as noted previously,³⁵ Te chemistry in silica is probably simpler). The data in Fig. 6 are again taken from the very same TEM sample, after separating the size distribution corresponding to nanocrystals inside the central part of the implantation profile (average radius 4.4 nm) from the size distribution corresponding to nanocrystals outside of the latter (average radius 3.8 nm). The former is obviously complex, reflecting (but not completely erasing) the competing nucleation mechanisms due to Te chemistry; while the latter is practically lognormal, with a geometrical standard deviation of 1.5 as above. The memory loss of initial conditions inside the implantation profile is not as complete for Te as for the other chalcogens, but the additional effects of cluster dissolution, solute diffusion and clustering again lead to the lognormal size distribution.

IV. DISCUSSION

The existence of an asymptotic form of the nanocrystal size distribution after long-term annealing is a well-known property of relaxing systems; it is also well-known that the detailed shape of such a distribution depends on the microscopic growth mechanism. Binder's presentation¹⁷ of the asymptotic behavior emphasized the analogy of the ripening treatment in the two very different growth regimes—that of condensation and that leading to coagulation. He derived an equation describing the size distribution evolution assuming growth by condensation and coagulation. The evolution of the number of clusters of size l may be rewritten in the following schematic way:

$$\left. \frac{\partial n_l}{\partial t} \right|_{\text{tot}} = \nabla \vec{J} + \left. \frac{\partial n_l}{\partial t} \right|_{\text{coag}}. \quad (11)$$

The first term describes precipitation by condensation by monomers and very small clusters, where \vec{J} is the current of clusters in size space. The second term describes precipitation by coagulation in way analogous to Eq. (4). Binder shows how that the search for the asymptotic behavior is analogous in both growth regimes. One searches for a size distribution of the form

$$n_l(t) = t^y \tilde{n}(lt^{-x}) \quad t \rightarrow \infty, \quad (12)$$

where x and y are time exponents to be determined with the help of Eq. (11) and the mass conservation equation

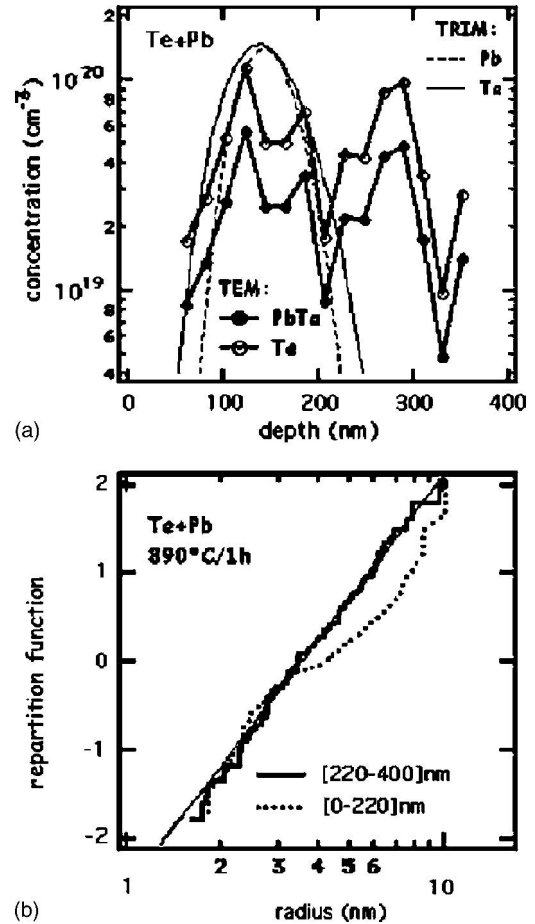


FIG. 6. (a) Comparison of initial concentration profiles of Pb and Te as determined by SRIM (thin lines, full and dashed) with precipitated element concentration as measured by TEM, assuming that all the precipitates are either PbTe (full dots) or Te (circles). Sample is Te+Pb sequentially implanted silica annealed 1 h at 890 °C. (b) Size repartition function in Gaussian coordinates as a function of depth in the Te+Pb sequentially implanted silica sample, after annealing 1 h at 890 °C. Two depth ranges were analyzed separately: 0–220 nm corresponds to the implanted profile (dotted line), and the other to greater depths (full line). Thin straight line, lognormal fit to nanocrystal radius repartition function for depths greater than 220 nm ($\sigma=1.4$).

$$\frac{d}{dt} \int_0^{\infty} n_l(t) l dl = 0. \quad (13)$$

Mass conservation thus leads to $y=-2x$, whether growth occurs by coagulation or condensation. The specific growth mechanisms only enter into account by taking either the first or the last term in Eq. (11). In the case of condensation driven by the surface tension effect (Gibbs-Thompson equation), one obtains an analytic equation which leads to the LSW form for \tilde{n} and $x=1/3$. In accordance with the LSW result, normalizing by the mean size allows one to write the size distribution as in Eq. (12). For coagulation, the equation verified by \tilde{n} is nonlinear and difficult to handle, but its solution has been shown^{19–21} to approximate a lognormal one when $t \rightarrow \infty$.

In the classical LSW description of ripening, there is a direct relation between the initial nanocrystal population, its spatial distribution and the precipitate size evolution. No nucleation occurs during ripening, and solute atoms travel between existing clusters. The clusters who have survived long term anneals were present in the initial stages of the ripening process. We have shown that in our implanted samples, after sufficient annealing (Figs. 2 and 3) the nanocrystal population and its spatial distribution bear no relation at all to the initial distribution. Therefore, the LSW ripening description does not apply at all to the present case. In other words, after ripening a homogeneous system conserves memory of its initial structure and may lead to the LSW size distribution, whereas in our inhomogeneous samples the memory is entirely lost, leading to a lognormal distribution. This relation between our results and a loss of information may be quantified as follows.

It is well known³⁶ that the amount of information contained in some distribution f may be evaluated by calculating its entropy:

$$S = - \int f \ln f. \quad (14)$$

Jaynes³⁷ showed that this applies to statistical physics: e.g., entropy is maximized at equilibrium, as expected from basic thermodynamics. It also applies to growth statistics, as discussed by Wang and Friedlander³⁸ who emphasized the similarity between asymptotic growth distributions and limiting values in the kinetic theory of gases. Rosen³⁹ first applied the entropy maximization principle to coagulation. Conservation equations [matter conservation via Eq. (13) and size space population conservation via Eq. (11)] provide constraints to be satisfied during the maximization procedure. In other words, the agreement between the experimental and the calculated size distribution depends on the amount of information supplied by the constraints. Under very general constraints on volume conservation, Rosen finds an asymptotic form

$$\tilde{n}(u) = \exp(-u) \quad (15)$$

where u is the normalized volume. It is a very good approximation to the lognormal distribution found by Friedlander, in the large-size limit ($u > 1$), whereas other constraints such as the evolution equation are needed in the small size regime.

May we reason in the same way as regards condensation? The results of Sec. III show that as major constraints on the nucleation and growth process are relaxed, the limiting shape of the size distribution becomes lognormal. This is summarized in Fig. 7, in which we compare our results to Eq. (15): excellent agreement is found, except for the smallest sizes where some reminiscence of the initial growth process remains. This is a strong indication that the discussion given above for coagulation may also be applied to condensation.

In order to obtain other distribution shapes—e.g., the LSW shape in the case of binary alloys—further constraints are required, such as that introduced by the Gibbs-Thomson surface tension criterion leading to LSW. Since the LSW

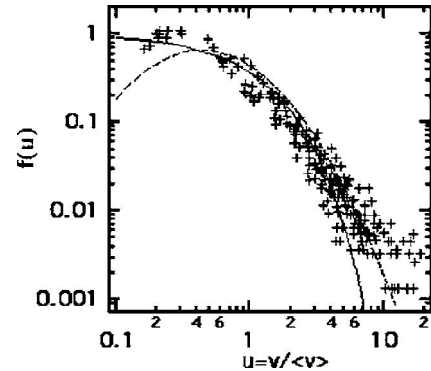


FIG. 7. Reduced volume (u) probability density plot. Crosses are experimental data for various semiconductor (PbS, PbSe, CdSe, PbTe) nanocrystals grown after sequential implantation of the components into pure silica (fluences ca. 10^{15} atoms cm^{-2}) at energies in the 100–300 keV range, and annealing in the range 800–900 °C for several hours. The full line is the maximum entropy distribution e^{-u} , determined by the sole constraint of volume conservation; the dashed line is the best fit of experimental data ($u > 1$) to the reduced lognormal distribution ($\mu=1$).

picture fails in our system (Sec. III), the volume conservation constraint alone is sufficient to approach the experimental distributions.

The constant value of the geometrical standard deviation of about 1.5 that we observed in our experiments was also found in aggregation studies by Gmachowski.⁸ Assuming a lognormal shape, he performed entropy maximization calculations of the most probable geometrical standard deviation that all led to values between 1.40 and 1.54, in spite of the broad variety of aggregate shapes and aggregation processes considered by him. The spread is rather narrow and the values are close to ours, again indicating that very little information may be deduced on the growth process from such size distribution shapes.

V. CONCLUSION

A general scheme of nanocrystal growth, at a given temperature, in a nonuniform concentration (e.g., implantation) profile may thus be described in the following way. As long as the slowest species remains inside the implantation profile, the shape of the size distribution is determined by the growth history (detailed nucleation conditions, diffusion, and reaction between species). In the homogeneous concentration case, diffusing solutes move upon annealing into regions where precipitates have already formed, and participate in Ostwald ripening leading to the LSW size distribution. When ion implantation is involved, the situation diverges from this picture because solutes out-diffusing from the implanted profile travel to a precipitate-free region where random nucleation screens the effect of surface tension, and leads to a lognormal shape with a geometrical standard deviation around 1.5. Alternatively, complex chemical reactions may produce the same result. The nucleation and growth history of the clusters is no longer revealed by the distribution shape: it is only contained in the geometrical average radius.

The lognormal distribution is only due to very general constraints on the system's evolution, such as matter conservation. Finally, we note that the lognormal shape is only a convenient approximation of the real size distribution, which may be approximated by other analytical forms.

In the case of narrow concentration profiles, nanocrystal size distribution control will only be possible for average sizes limited to a few nanometers; because they tend to provide a more uniform initial matter distribution, multienergy implants allow control over a greater size range, as found empirically in past experiments.

ACKNOWLEDGMENTS

We are very grateful to K. H. Heinig for critical discussions, and to O. Kaitasov and S. Collin for technical assistance.

APPENDIX: A PROCEDURE TO DETERMINE NANOCRYSTAL DENSITIES AND SIZE DISTRIBUTIONS

In order to determine the nanocrystal depth and size distributions from TEM images, we set up a procedure to minimize bias in the determination of the nanocrystal radii and integrated matter depth dependences. Since we deal with

samples involving inhomogeneous solute concentrations, nucleation does not occur uniformly in depth. Hence, special care was taken to acquire images of TEM cross sections in which the SiO₂ or glass surface was parallel to one side of the frame. As TEM samples usually do not have a uniform thickness, the background gray level in the corresponding images show variations that can bias the nanocluster radius measurement, depending on the nanocrystals' position in the layer. To obviate this problem, we first applied a Sobel-type gradient operator to all frames before measuring the nanocrystals' size and position. The nanocrystal density was such that there were no overlapping nanocrystal images at typical sample thicknesses. Hence, all nanocrystal radii, depth and precipitated matter concentrations could be compiled. On a TEM micrograph, only a surface density of nanocrystals (i.e., surface concentration projected on the image plane along the electron beam direction) is measured. The thickness of the cross-section sample, unless specified otherwise, was taken to be 100 nm. In order to determine the precipitated matter concentration, the nanocrystal volumes (deduced from their radius) were summed in a given depth slice, and then divided by the average TEM cross-section thickness and the number of crystalline units per volume (19.1 PbS nm⁻³; 14.9 PbTe nm⁻³).

*Corresponding author. Electronic address: bernas@csm.in2p3.fr

- ¹S. V. Gaponenko, *Optical Properties of Semiconductor Nanocrystals* (Cambridge University Press, Cambridge, U.K., 1998).
- ²B. O. Dabbousi, J. Rodriguez-Viejo, F. V. Mikulec, J. R. Heine, H. Mattoussi, R. Ober, K. F. Jensen, and M. G. Bawendi, *J. Phys. Chem. B* **101**, 9463 (1997).
- ³A. Sashchiuk, E. Lifshitz, R. Reisfeld, T. Saraidarov, M. Zelner, and A. Willenz, *J. Sol-Gel Sci. Technol.* **24**, 31 (2002).
- ⁴I. M. Lifshitz and V. V. Slyosov, *J. Phys. Chem. Solids* **28**, 35 (1961).
- ⁵C. Wagner, *Z. Elektrochem.* **65**, 58 (1961).
- ⁶R. Espiau de Lamaestre, J. Majimel, F. Jomard, and H. Bernas, *J. Phys. Chem. B* **109**, 19148 (2005).
- ⁷E. Limpert, W. A. Stahel, and M. Abbt, *BioScience* **51**, 341 (2001) and references therein; see <http://www.inf.ethz.ch/personal/gut/lognormal/>.
- ⁸L. Gmachowski, *Colloids Surf., A* **176**, 151 (2001); **201**, 41 (2002).
- ⁹C. S. Graham and A. J. Robinson, *J. Aerosol Sci.* **7**, 261 (1976).
- ¹⁰S. Yatsuya, S. Kasukabe, and R. Uyeda, *Jpn. J. Appl. Phys.* **12**, 1675 (1973).
- ¹¹C. G. Granqvist and R. A. Buhrman, *J. Appl. Phys.* **47**, 2200 (1976).
- ¹²A. Miotello, G. De Marchi, G. Mattei, P. Mazzoldi, and C. Sada, *Phys. Rev. B* **63**, 075409 (2001).
- ¹³E. Borsella, M. A. Garcia, G. Mattei, C. Maurizio, P. Mazzoldi, E. Cattaruzza, F. Gonella, G. Battaglin, A. Quaranta, and F. D'Acapito, *J. Appl. Phys.* **90**, 4467 (2001).
- ¹⁴H. H. Andersen and E. Johnson, *Nucl. Instrum. Methods Phys. Res. B* **106**, 480 (1995).

- ¹⁵S. Hagège and U. Dahmen, *Philos. Mag. Lett.* **74**, 259 (1996), and reference therein.
- ¹⁶E. Valentin, H. Bernas, C. Ricolleau, and F. Creuzet, *Phys. Rev. Lett.* **86**, 99 (2001); E. Valentin, Ph.D thesis, Ecole Centrale de Paris, 1999.
- ¹⁷K. Binder, *Phys. Rev. B* **15**, 4425 (1977).
- ¹⁸M. von Smoluchowski, *Phys. Z.* **17**, 585 (1916).
- ¹⁹S. K. Friedlander and C. S. Wang, *J. Colloid Interface Sci.* **22**, 126 (1966).
- ²⁰D. L. Swift and S. K. Friedlander, *J. Colloid Sci.* **19**, 621 (1964).
- ²¹G. M. Hidy, *J. Colloid Sci.* **20**, 123 (1965).
- ²²P. T. Spicer and S. E. Pratsinis, *Water Res.* **30**, 1049 (1996).
- ²³C. S. Graham and A. J. Robinson, *J. Aerosol Sci.* **7**, 261 (1976).
- ²⁴R. Jullien, *New J. Chem.* **14**, 239 (1990).
- ²⁵J. Söderlund, L. B. Kiss, G. A. Niklasson, and C. G. Granqvist, *Phys. Rev. Lett.* **80**, 2386 (1998).
- ²⁶H. Trinkaus and S. Mantl, *Nucl. Instrum. Methods Phys. Res. B* **80/81**, 862 (1993).
- ²⁷V. A. Borodin, *Physica A* **211**, 279 (1994).
- ²⁸V. A. Borodin, K. H. Heinig, and S. Reiss, *Phys. Rev. B* **56**, 5332 (1997).
- ²⁹R. Espiau de Lamaestre and H. Bernas, *J. Appl. Phys.* **98**, 104310 (2005).
- ³⁰R. Espiau de Lamaestre, H. Bernas, and F. Jomard, *Nucl. Instrum. Methods Phys. Res. B* **216**, 402 (2004).
- ³¹A. Meldrum, E. Sonder, R. A. Zuhr, I. M. Anderson, J. D. Budai, C. W. White, L. A. Boatner, and D. O. Henderson, *J. Mater. Sci.* **14**, 4489 (1999).
- ³²C. Bonafos, B. Garrido, M. Lopez, A. Romano-Rodriguez, O. Gonzales-Varona, A. Perez-Rodriguez, and J. R. Morante, *Appl.*

- Phys. Lett. **72**, 3488 (1998).
- ³³R. Espiau de Lamaestre, Ph.D. thesis, University Paris XI, 2005.
- ³⁴N. L. Johnson and S. Kotz, *Distributions in Statistics—Continuous Univariate Distributions* (John Wiley & Sons, New York, 1970), Vol. 1, pp. 112—136.
- ³⁵R. Espiau de Lamaestre, F. Jomard, J. Majimel, and H. Bernas, J. Non-Cryst. Solids **351**, 3031 (2005).
- ³⁶C. E. Shannon, Bell Syst. Tech. J. **27**, 379 (1948); **27**, 623 (1948).
- ³⁷E. T. Jaynes, Phys. Rev. **106**, 620 (1957); **108**, 171 (1957).
- ³⁸S. K. Friedlander and C. S. Wang, J. Colloid Interface Sci. **24**, 170 (1967).
- ³⁹J. M. Rosen, J. Colloid Interface Sci. **99**, 9 (1984).